Design and development of nanocomposites by carbon-based 2D materials for piezoresistive sensing application

by

Yasaman Rahimidarestani

A thesis

presented to the University of Waterloo

in fulfillment of the

thesis requirement for the degree of

Master of Applied Science

in

Chemical Engineering (Nanotechnology)

Waterloo, Ontario, Canada, 2023

© Yasaman Rahimidarestani 2023

Author's Declaration

I hereby declare that I am the sole author of this thesis. This is a true copy of the thesis, including any required final revisions, as accepted by my examiners.

I understand that my thesis may be made electronically available to the public.

Abstract

In the realm of wearable electronic devices, considerable attention has been directed toward flexible compressive piezoresistive sensors, given their potential applications in real-time human health monitoring and gesture recognition for robotics. Development of such sensors using electrically conductive polymer nanocomposites (E-CPnC) holds great promise due to their remarkable characteristics such as lightweightness and cost effectiveness. Despite notable advancements in this field, the fabrication techniques for compressive polymer-based piezoresistive sensors still tend to rely on complex and multi-step processes. This highlights the urgent need for developing facile and cost-effective manufacturing methods to propel advancements in the electronic industry.

In this research we address the growing demand for facile and cost-effective manufacturing methods in the development of compressive piezoresistive sensors for wearable electronic devices. This study introduces a novel one-pot soft-templating method for fabricating PDMS-based conductive compressive sensors, benefiting the unique physical properties of cyclohexane. By controlling temperature and pressure conditions, a microcellular structure was prepared through the solvent's crystals sublimation, effectively serving as a soft template. Graphene, chosen for its conductive properties, was dispersed in varying proportions of cyclohexane, with the addition of PDMS and its curing agent. The solution freeze-dried, and the rapid evaporation of cyclohexane solid crystals within the structure coupled with the crosslinking of PDMS facilitated the creation of pores. Consequently, diverse microcellular structures with varying levels of porosity were successfully fabricated.

For investigating the morphology of the resulting microcellular nanocomposites scanning electron microscopy (SEM) was used. The electrical conductivity, dielectric properties, and sensitivity of the nanocomposites could be analyzed through electrochemical impedance spectroscopy (EIS) and EIS coupled with universal testing machine (UTM). The mechanical performance, considering the stress-strain curves, mechanical strength, Young’s modules and the fatigue testing were analyzed by UTM. The fabricated sensors exhibit remarkable electrical conductivity, mechanical strength and sensitivity that can be achieved through the optimization of graphene concentration in the microcellular structure. Optimization of solvent concentration led to the attainment of varied pore sizes and void fractions. When 0.43 vol% graphene was introduced, the microcellular nanocomposite displayed an electrical conductivity of 2.5×10^{-2} S/m and a mechanical strength of 780 kPa at 85% compression strain. This remarkable compressibility was attributed to the robust 3D interconnected structure featuring a high

void fraction of 82%. With an increase in graphene concentration to 0.87 vol%, the electrical conductivity rose to 35×10^{-2} S/m, and the compressive strength reached 1500 kPa at 70% strain, accompanied by a void fraction of 64.8%. Moreover, the electromechanical performance analysis reveals two linear resistance responses along the compressive strain range, demonstrating the versatility of the sensors in capturing different levels of compression. For instance, the foam loaded with 0.43 vol% exhibited a notable change in resistivity up to 10% strain, resulting in a high gauge factor of 0.5 kPa^{-1}. From 10 to 85% strain, the foam displayed a second linear detection region with a gauge factor of 1.2 MPa^{-1}. The compressive sensors demonstrated a rapid response time of 20 ms and exceptional cyclic stability of 500 cycles, owing to their resilient 3D interconnected structure, indicating their suitability for mid and high-pressure (10 kPa- 1 MPa) sensing applications, as well as real-time monitoring of human joint movements.

Keywords: conductive polymeric composites, microcellular structures, electrical conductivity, carbonaceous nanomaterials, soft-templating, one-pot synthesis, piezoresistive sensors, physical tactile sensors, wearable electronics

Acknowledgements

I express my sincere gratitude to Professor Aiping Yu, my supervisor, for granting me the opportunity to conduct research within an international group. Special appreciation goes to Professor Micheal Pope and Milad Kamkar, my committee members, whose inspiration, advice, and support provided invaluable insights to grow as a research scientist.

I extend heartfelt thanks to my colleagues and friends, Dr. Saeed Habibpour, Dr. Kiyoumars Zarshenas, Dr. Rasool Nasseri, and Yasaman Maddah. Their assistance, guidance, and engaging discussions were instrumental during challenging phases of my academic journey. I would like to specially thank Saeed, who is more than a colleague to me. He has been the source of encouragement, inspiring me to think deeply about every situation and overcoming barriers in my academic career by having a belief in myself. I have learned a tremendous amount from him.

Lastly, my deepest appreciation goes to my family for their unwavering love and encouragement throughout this endeavor. This achievement would not have been possible without the enduring support of my family. Their sacrifices, understanding, and belief in my aspirations have been instrumental in shaping my academic success.

Dedication

In loving dedication to my parents, Jahanbakhsh and Manijeh, whose love and encouragement have been the fuel for my dreams, and the steady anchors in the storms of life. They are the unsung heroes behind every late-night study session and every milestone I've reached in my life. They are the ones who give me courage to follow my dreams far away from the place we call "Home". Mummy and Daddy, your sacrifices, encouragement, and unconditional love have been the driving force of my academic journey. This thesis is as much yours as it is mine. I love you beyond words can express.

Table of Contents

Author's Declaration ii

Abstract iii

Acknowledgements v

Dedication vi

List of Figures x

List of Tables xi

List of Abbreviations xii

List of Symbols xv

Chapter 1 Introduction 1

1.1 Background 1

1.2 Study Objectives and Approach 3

1.3 Thesis Outline 4

Chapter 2 Background and Literature Review 5

2.1 Summary 5

2.2 Electrical Properties: Concept, Measurement and Dielectric Insights 5

2.2.1 Electrical Conductivity 5

2.2.2 Electrical Conductivity Measurement 6

2.2.3 Dielectric Properties 7

2.3 Electrically Conductive Polymer Nanocomposites (E-CPnCs) 8

2.3.1 E-CPnC based physical sensors 8

2.3.2 Components of Flexible E-CPnCs 13

2.3.3 Fabrication Methods of Flexible E-CPnCs 18

2.3.4 Multifunctional Microcellular E-CPnCs 20

2.4 Conclusions and Future Perspectives 22
Chapter 3 Characterization Techniques 23
3.1 X-ray Diffraction (XRD) 23
3.2 Raman Spectroscopy 24
3.3 X-ray photoelectron spectroscopy (XPS) 24
3.4 Scanning Electron Microscopy (SEM) 25
3.5 Mechanical Properties 25
3.6 Electrochemical Analysis 26
Chapter 4 Fabrication of Cellular Electrically Conductive Graphene-PDMS based Composite through Novel One-pot Synthesis 29
4.1 Introduction 29
4.2 Experimental Section 29
4.2.1 Materials and chemicals: 29
4.2.2 Synthesis of conductive graphene 30
4.2.3 Fabrication of 3D porous graphene-PDMS foam: 31
4.3 Characterization 33
4.3.1 Morphology and physiochemical analysis of nanomaterials 33
4.3.2 Characterization, electrical and mechanical performance of fabricated sensors 33
4.4 Results and Discussion 35
4.4.1 Nanomaterials characterization 35
4.4.2 Characterization of G-PDMS foams 37
4.4.3 Electrical Conductivity of G-PDMS sensors. 39
4.4.4 Mechanical properties of G-PDMS sensors 45
4.4.5 Fatigue resistance and piezoresistivity testing of G-PDMS70 47

4.5 Conclusion 49

Chapter 5 Conclusion and Recommendations 52

5.1 Conclusions 52

5.2 Recommendations 53

5.2.1 Material research 54

5.2.2 Processing research 54

I. Assessing the impact of nanomaterial orientation on electromechanical and EMI SE properties of microcellular networks 55

II. Investigating impact of gradient porosity and conductivity on microcellular nanocomposites properties 55

References 56

List of Figures

Figure 1.1 Expected flexible electronic market size in USD billion from 2022 to 2032 (left hand side), expected market size in USD billion for flexible sensors from 2022 to 2032 (right hand side)[7,8]..... 1
Figure 2.1 Schematic illustration of electrical conductivity measurement setup of (a) two-point probe (b) four-point probe (c) through-plane (d) in-plane..... 7
Figure 2.2. Schematic of shielding mechanisms by a shielding material[109]. 21
Figure 4.1 Schematic illustration of graphene production process..... 31
Figure 4.2 Schematic illustration of 3D microcellular graphene-PDMS preparation process. 32
Figure 4.3 Home-made density measurement apparatus. 35
Figure 4.4 (a) XRD graphs (b) Raman Spectra (c-d) C1s high resolution XPS of GO and graphene sheets, and SEM images of (e-f) graphite and (g-h) graphene. 37
Figure 4.5 SEM images of G-PDMS foams, (a1-a2) SEM images of G-PDMS87 with 250X and 1000X magnification, (b1-b2) SEM images of G-PDMS70 with 250X and 1000X magnification, (c1-c2) SEM images of G-PDMS43 with 250X and 1000X magnification. 39
Figure 4.6 (a) DC electrical conductivity, (b) broadband AC electrical conductivity, (c) real permittivity, (d) dielectric loss, (e) comparison of dielectric properties at the frequency of 10^3 Hz for G-PDMS foams, and (f) resistance change curves of G-PDMS foams under compressive strains..... 45
Figure 4.7 Compressive stress-strain curve of (a) G-PDMS87, (b) G-PDMS43, and (c) G-PDMS70. 46
Figure 4.8 Cyclic compressive stress-strain curves for G-PDMS70 with the rate of 3 mm.min-1 under maximum compressive strain of 30%, (b) Cyclic compressive testing at the maximum compressive strain of 30% for G-PDMS70, (c) extracted parameters of cyclic testing for G-PDMS70. 48
Figure 4.9 (a) 5 cyclic compression-electric sensing curve of G-PDMS70 with different compression rate at fixed 30% compressive strain, (b) actual piezoresistive sensing performance by tap testing. .. 49

List of Tables

Table 2.1 Physical properties of conductive nanofillers [89,90]. 17
Table 4.1 Physical properties of G-PDMS foams. 32
Table 4.2 Extracted parameters from the XRD and Raman graph. 37
Table 4.3 Physical properties of G-PDMS foams. 39
Table 4.4 Extracted parameters from mechanical testing. 47
Table 4.5 Comparison of results with other microcellular graphene-based polymer nanocomposites in literature 50

List of Abbreviations

2D	Two-dimensional
3D	Three-dimensional
A	Absorption
A	Cross sectional area
Ar	Argon gas
AC	Alternating Current
C	Current
CB	Carbon Black
CNT	Carbon Nanotube
CNF	Carbon Nanofiber
CA	Chronoamperometry
CV	Cyclic Voltammetry
CPnC	Conductive Polymer Nanocomposite
E-CPnC	Electrically Conductive Polymer Nanocomposite
DRS	Dielectric Relaxation Spectroscopy
DMF	Dimethylformamide
DC	Direct Current
DI	Deionized
EIS	Electrochemical Impedance Spectroscopy
EM	Electromagnetic
EMI	Electromagnetic Interference

EDX	Energy Dispersive X-ray Spectroscopy
FTIR	Fourier Transform Infrared Spectroscopy
FWHM	Full Width at Half Maximum
GF	Gauge Factor
GNR	Graphene Nanoribbon
GO	Graphene Oxide
GONR	Graphene Oxide Nanoribbon
HMI	Human-Machine Interaction
LSV	Linear Sweep Voltammetry
MWCNT	Multiwalled Carbon Nanotubes
MX	MXene
PCM	Planetary Centrifugal Mixer
P	Pressure
PDMS	Polydimethylsiloxane
PVA	Polyvinyl alcohol
PVP	Polyvinylpyrrolidone
PU	Polyurethane
rGNR	Reduced Graphene Nanoribbon
R	Reflection
SEM	Scanning Electron Microscope
SE	Shielding Effectiveness
SS	Strain-Stress
t	Thickness

TPU	Thermoplastic Polyurethane
T	Transmission
UDR	Universal Dynamic Response
UTM	Universal Testing Machine
V	Voltage
XRD	X-ray Diffraction
XPS	X-ray photoelectron spectroscopy

List of Symbols

Å	Angstrom
ω	Angular Frequency
L_x	Average Number of Layers
ρ_b	Bulk Density of Composite
τ	Crystal Size
ρ_f	Density of Filler
ρ_m	Density of Matrix
ρ_w	Density of Water
tan δ	Dielectric Loss
ε'	Dielectric Permittivity
σ	Electrical Conductivity
ψ	Energy Loss Coefficient
σ_f	Filler Conductivity
β	Full Width at Half Maximum
ε''	Imaginary Part of the Dielectric Permittivity
θ	Incident angle of XRD
R_0	Initial Resistance
L_a	Inter-Defect Distance
L_c	Inter-Layer Distance
Ω	Ohms
R	Resistance
ρ	Resistivity

$\Delta R/R_0$	Resistance Variation (proportional change in resistivity)
S	Siemens
ε	Strain
ρc	True Density of graphene
ν	Velocity
Vc	Volume percent of nanomaterials in composite
λ	Wavelength
m_a	Weight of the foam measured in the air
m_w	Weight of the foam immersed in the water
Wc	Weight fraction of nanomaterials in composite
Uc	Work of compression of stress-strain curves
Ur	Work of recovery of stress-strain curves

Chapter 1
Introduction

1.1 Background

The world today heavily relies on electronic devices, which have become an integral part of our daily lives. From smartphones and laptops to smart watches and home appliances, electronic devices are ubiquitous and highly prevalent in modern society. As the electronics industry has continued to expand since 1950s, there is a growing demand for devices that offer multiple functionalities[1,2]. To meet this demand, fabricated materials have evolved from rigid and bulky metals and semiconductors to more flexible and lightweight ones that can be processed using simple manufacturing techniques. This evolution has given rise to a new generation of electronic devices with diverse applications in areas such as sensors[3], energy storage[4], energy harvesting[5], and electromagnetic interference (EMI) shielding[6].

According to the Figure 1.1a, the assessed value of the worldwide flexible electronics market reached USD 29 billion in the year 2022, with projections indicating a prospective expansion to approximately USD 71.54 billion by the year 2032. In this regard, the share of global flexible sensors market was estimated to be USD 9.13 billion in 2022 and is predicted to reach USD 19.44 billion by 2032, as depicted in Figure 1.1b. The increasing trend reflects the widespread adoption of flexible sensors in our daily lives, contributing to a healthier and more convenient lifestyle.

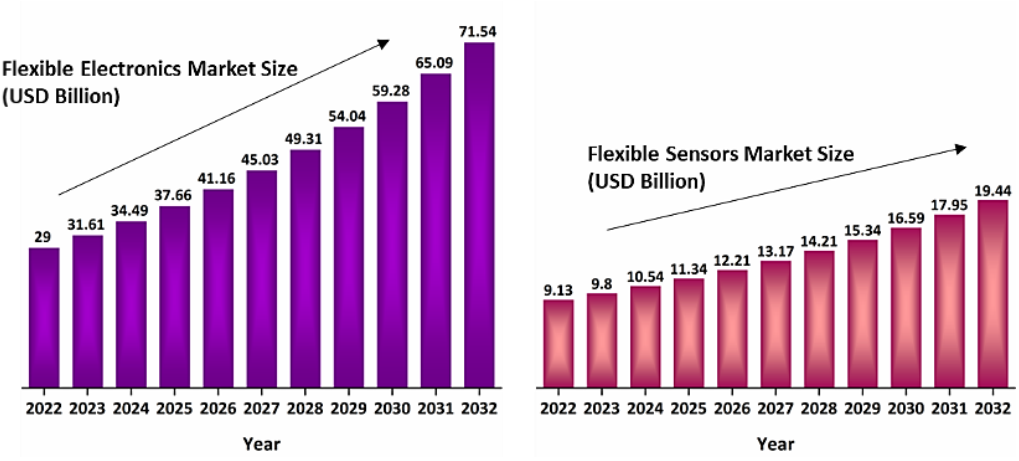


Figure 1.1 Expected flexible electronic market size in USD billion from 2022 to 2032 (left hand side), expected market size in USD billion for flexible sensors from 2022 to 2032 (right hand side)[7,8].

To address the increasing demand for multifunctional flexible electronic devices, novel materials have been developed, including electrically conductive polymer nanocomposites (E-CPnCs)[9]. These nanocomposites consist of a matrix with conductive nanomaterials, resulting in a unique combination of properties from both phases. For instance, polymers as a matrix provide excellent mechanical performance, flexibility, chemical stability, and corrosion resistance to the nanocomposites. Additionally, these lightweight materials can be easily processed in fabrication steps. Notably, carbonaceous nanomaterials, as conductive nanofillers, exhibit outstanding electrical and thermal conductivity, remarkable mechanical strength, and excellent chemical stability. These features make them promising candidates for the development of electronic devices, including wearable sensors[9,10]. When it comes to sensor application, key features such as sensitivity, fast response time, reliability, and mechanical robustness are of utmost importance[11]. Electrically conductive polymer nanocomposites demonstrate excellent electrical conductivity as well as flexibility and outstanding mechanical stability, making them highly desirable for mechanical sensing applications.

Flexible physical sensors, including both strain and pressure sensors, have garnered considerable attention due to their versatile applications across various fields. These devices generate electric signals when subjected to mechanical forces, utilizing electrically conductive nanofillers within composites to provide the electrical signal, while the polymeric matrix serves as the flexible material enabling mechanical deformation. These flexible sensors find application in diverse areas, including human-machine interaction (HMI)[12–14], flexible robotics[15–17], artificial intelligence[1,18], E-Skin [19,20] and health care[21–24]. Numerous methods have been developed to produce nanocomposites, tailored to suit specific materials and application domains. For instance, for designing stretchable sensors, conductive nanomaterials can be incorporated into the polymeric elastomers using several processing methods, such as solution blending and melt mixing [25–27]. Compressive sensors, in particular, are designed based on microcellular structures that incorporate porosity, allowing for compression upon applying pressure. Similarly, compressive sensors can be fabricated through different techniques, including batch foaming, freeze-casting, or the utilization of templates to develop cellular structures[28].

Compressible physical sensors have garnered significant attention for their remarkable properties. Notably, their structure is easily tunable, and they exhibit lower density and prolonged workability compared to stretchable sensors. Unlike stretchable sensors, which may lose functionality after prolonged exposure to large strains and struggle to recover to their initial state, compressible sensors

can withstand larger deformations and recover effectively due to their low hysteresis deformability[29]. Moreover, the microcellular structure of compressible sensors contributes to their adsorption capabilities within their pores. Consequently, these sensors find multifunctional applications, serving as materials for contamination removal and EMI shielding. They could effectively attenuate EM waves by incorporating high absorbent shielding mechanism. While various methods for fabricating E-CPnC based pressure sensors have been developed, they typically involve a two-step and complex process. The primary objective is to create pores within the structure, achieved through methods such as the batch foaming process, where carbon dioxide is purged within the bulk nanocomposite to form pores. Alternatively, porous structures can be created using templates, followed by a step to remove the template. Recognizing the need for a more straightforward, one-step fabrication method for constructing 3D microcellular E-CPnCs as pressure sensors with high sensitivity and excellent mechanical performance, we aim to design and develop a facile method for microcellular structure fabrication without the subsequent need for template removal.

Researchers have extensively explored ways to enhance the functionality of physical sensors, focusing on improving both sensitivity and mechanical robustness. Simultaneously, there have been efforts to advance the multifunctionality of flexible sensors, particularly those integrated into single devices, such as sensors capable of functioning as EMI shielding materials[30–32]. It is crucial to recognize that accomplishing these objectives necessitates research on designing E-CPnCs. These advanced capabilities can be engineered through a combination of material control and process control methodologies during the fabrication of E-CPnCs. Therefore, our focus was on designing and developing strategies to achieve this goal. Considering the unexplored potential of processing methodologies for microcellular E-CPnCs in physical sensing technology, they serve as a compelling catalyst for the pursuit of this research.

1.2 Study Objectives and Approach

This project has a primary objective of designing, developing, and characterizing innovative electrically conductive nanocomposites for applications in tactile sensing technology. Throughout this research, a unique fabrication processing method was devised for the creation of compressive piezoresistive sensors based on E-CPnCs. To address the complexity and drawbacks of the existing processing techniques for microcellular structures, a novel one-pot processing method known as the soft templating

method was introduced in this project. As a result, microcellular E-CPnCs were synthesized using the soft templating method, incorporating 2D graphene conductive nanofillers and polydimethylsiloxane (PDMS) as a flexible matrix. Cyclohexane was used as a solvent to disperse polymer and nanofillers, while also acting as a soft template to form a 3D porous structure without requiring additional steps for its removal. Taking advantage of the physical properties of cyclohexane, which evaporates at low pressure, pores were created within the structure in a single step during the fabrication process. As a result, cyclohexane evaporation leads to pore formation in the composite, along with crosslinking of PDMS results in a robust 3D microcellular network. The graphene-PDMS based compressive sensors were subjected to study for their electrical, mechanical, and electromechanical properties in this research.

1.3 Thesis Outline

Overall, the focus of this thesis is on design and development of E-CPnCs serving as piezoresistive sensors, which comprises five chapters. In Chapter 1, readers are presented with background information and an exploration of the imperative need for the proposed work. Chapter 2 offers a concise overview and literature review of E-CPnCs, their components and fabrication process, and their applications in flexible electronic devices, with a specific focus on tactile physical sensors. This chapter also delves into the fundamental parameters influencing physical sensors and their operating mechanisms. Chapter 3 is dedicated to the methodology employed and the characterization techniques utilized for investigating the characteristic properties and performance of cellular E-CPnCs. Moving forward, Chapter 4 provides detailed examination and discussion on the novel soft templating method employed for fabricating cellular compressive sensors. It further investigates the electrical, mechanical, and electromechanical performance of fabricated compressive piezoresistive sensors. In the concluding Chapter 5, a summary of the results is provided, highlighting the key aspects of characteristic and performance of fabricated compressive piezoresistive sensors. Additionally, this chapter explores potential insights for the development of cellular E-CPnCs used as piezoresistive sensors, thereby offering a comprehensive conclusion to the thesis.

Chapter 2
Background and Literature Review

2.1 Summary

In this chapter, a background of electrical properties, literature review about electrically conductive polymer nanocomposites (E-CPnC) and their components in physical sensors are presented. A variety of methods used for fabrication of flexible E-CPnCs are also reviewed in this chapter.

2.2 Electrical Properties: Concept, Measurement and Dielectric Insights

2.2.1 Electrical Conductivity

Electrical conductivity (σ) is a fundamental property of materials that is defined as the amount of charged particles (such as electrons) a material can carry. It is influenced by the concentration of charge carriers, their mobility, and the structural features of the material. Expressed by Equation 2.1, electrical conductivity is reciprocal of resistivity (ρ) which is defined as how strongly a material can oppose the electric flow[33].

$$\boldsymbol{\sigma = \frac{1}{\rho}} \tag{2.1}$$

The units of material's electrical resistivity and electrical conductivity are mainly measured in ohmmeters (Ω.m) and siemens per meter (S/m), respectively.

The resistivity of materials has a proportional relation with the material's resistance (R), given by Equation 2.2.

$$\boldsymbol{\rho = \frac{RA}{l}} \tag{2.2}$$

In this equation, ρ represents resistivity, R is the resistance, *A* is the cross-sectional area perpendicular to the direction of the current and *l* is the length between the two points at which the current flows.

The resistance (R) is also determined by the Ohm's law, which relates the current (I), the voltage (V), and the resistance (R) as defined in Equation 2.3.

$$\textbf{Current}\ (\mathbf{I}, \mathbf{A}) = \frac{\textit{Voltage}\ (V,V)}{\textit{Resistance}\ (R,\Omega)} \quad 2.3$$

This equation states that the magnitude of electrical current flowing through fixed points is directly proportional to the voltage applied across it, and inversely proportional to the resistance.

2.2.2 Electrical Conductivity Measurement

There are several techniques available to measure electrical conductivity, including two-point probe method, four-point probe method and impedance spectroscopy[34]. Figure 2.1a presents a schematic of two-point probe method in which two probes are placed on a sample material and a voltage is applied across them. The resulting current is measured, and the conductivity of the sample is calculated using Ohm's law. This method is relatively simple and inexpensive, but it is more sensitive to the contact resistance between the sample and the probe and less accurate than the four-point probe method. Figure 2.1b presents four-point probe method in which four equally spaced electrical probes are placed on a flat surface of a material, and the voltage is measured between two inner probes while current passing between two outer probes. In this way, the electrical conductivity of the sample can be calculated more accurately with less sensitivity to contact resistance by using a more expensive and sophisticated measurement setup. Thus, this method is preferable for measuring electrical conductivity, especially thin films, coatings, and materials with low electrical conductivity. Impedance spectroscopy is another method which involves measuring the impedance of the material over a range of frequencies to calculate the conductivity. It is a useful method for measuring frequency-dependent conductivity of materials, specifically semiconductors.

Electrical conductivity can also be measured in different directions based on the probe arrangement, known as through-plane (Figure 2.1c) and in-plane (Figure 2.1d) for analyzing material's behavior in different orientation and configuration. In-plane testing (sheet-resistance testing) involves measuring the conductivity of a material parallel to the surface, while through-plane testing involves measuring the conductivity of a material in a direction perpendicular to the surface. Thus, the probes are positioned on one side of a sample for in-plane testing and on each side of a sample for through-plane conductivity measurement.

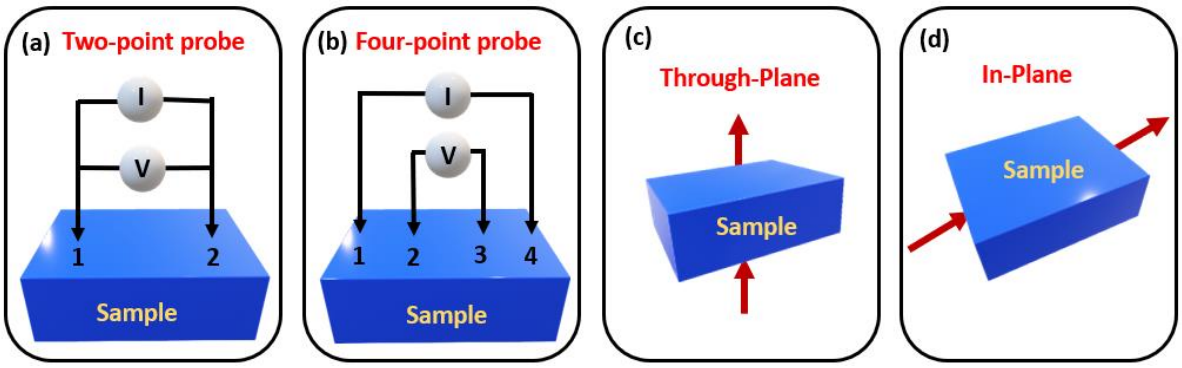


Figure 2.1 Schematic illustration of electrical conductivity measurement setup of (a) two-point probe (b) four-point probe (c) through-plane (d) in-plane.

2.2.3 Dielectric Properties

Dielectric properties are essential for determining the electrical performance of materials, including dielectric constant, dielectric loss, and breakdown strength. It is an essential parameter used for design and development of electrically conductive nanocomposites. Dielectric constant, also known as the relative permittivity, is a measure of the material's ability to store electrical energy when an electric field is applied. The dielectric loss, on the other hand, is a measure of the energy dissipated by the material due to the frictional heating caused by the movement of electrical charges. Finally, the breakdown strength refers to the voltage at which the material breaks down and becomes conductive, leading to a loss of its insulating properties[35].

Dielectric constant can be defined as a complex function as below (Equation 2.4):

$$\boldsymbol{\varepsilon(\omega) = \varepsilon'(\omega) - i\varepsilon''(\omega)} \qquad 2.4$$

where ω is the angular frequency, ε'(ω) is the real part, and ε''(ω) is the imaginary part of the dielectric permittivity. Dielectric loss (tan δ) defines as the ratio of imaginary part to real part ($\varepsilon'' / \varepsilon'$).

In order to design nanocomposites for energy storage applications, high permittivity (ε') and low dielectric loss (tan δ) is favorable. Ceramics, as traditional dielectric materials, have excellent dielectric properties, high stiffness, and thermal stability. However, they have limited practical use in electronic devices due to their poor flexibility, high-density, and challenging processing conditions. As a result, researchers have turned to polymeric dielectrics as alternative materials. Polymeric dielectrics offer the

advantage of tunable dielectric properties with low dielectric loss and high dielectric breakdown strength [36]. Besides, they can also be molded into various configurations more easily due to their mechanical flexibility which makes them suitable for electronic devices that require reduced volume and weight. Incorporation of conductive or non-conductive fillers inside polymer matrix can improve polymer composites' dielectric properties.

2.3 Electrically Conductive Polymer Nanocomposites (E-CPnCs)

Electrically conductive polymer nanocomposites (E-CPnCs) are a class of materials that have emerged as a promising candidate for large production of new generation electronic devices. These nanocomposites consist of a polymeric matrix with added conductive nanofillers, such as carbonaceous nanomaterials. The resulting nanocomposite exhibits a unique combination of properties. Polymers as light weight, low density and easily processable materials offer numerous advantages, such as exceptional mechanical properties, flexibility, chemical stability, and corrosion resistance to E-CPnCs. Additionally, carbonaceous nanomaterials demonstrate impressive electrical and thermal conductivity, remarkable mechanical strength, and exceptional chemical stability. Therefore, conductive polymer nanocomposites have found widespread use in the manufacturing of sensors, energy storage devices, and EMI shielding materials[37].

2.3.1 E-CPnC based physical sensors

Sensors play a crucial role in various industries and applications by enabling the detection and measurement of physical, chemical, and biological parameters. They provide valuable information for monitoring, control, and decision-making processes. Based on the signal type, they are mainly divided into electrophysiological, physical, and chemical sensors. Electrophysiological sensors measure electrical potential differences between electrodes. Physical sensors measure changes in electrical properties triggered by mechanical, temperature, or optical stimuli. Chemical sensors quantify analytes (including ions, molecules, or proteins) using active materials designed to respond to specific chemical species [38]

In recent years, there has been significant interest in the development of wearable physical sensors, particularly for human health monitoring. For instance, sensors dedicated to monitoring blood pressure, body temperature, and recognizing posture have been created for analyzing human health conditions,

as well as assessing muscle and skin stretching and exercise performance. Among physical sensors, flexible tactile sensors stand out as a type of physical sensor functioning based on their sensitivity to mechanical stimuli, including stretchable sensors and compressive sensors. They find broad applications, not only in the automation industry, such as pressure sensors, but also in human motion detection, notably in the analysis of posture recognition during exercise[39]. Physical tactile sensors mainly work based on piezoresistive, piezoelectric and capacitive sensing mechanism [40–42]. The piezoresistive sensing mechanism is based on converting mechanical stimuli into electronic signals by changing the electrical resistivity within the system. Abrupt changes in the conductivity by an applied mechanical force can be subsequently processed and interpreted by remote devices. They offer simple working principles while fabricated through simple techniques. Similarly, capacitive sensors convert mechanical stimuli into a change in the capacitance value. They provide the benefits of quicker response times and reduced power consumption compared to piezoresistive sensing mechanism. Piezoelectric sensors are mainly fabricated by integration of semiconducting materials, such as zinc oxide, cadmium sulfide and gallium nitride. Dielectric material experiences deformation from external forces acting in a specific direction, like bending or telescopic deformation. This process induces polarization of internal charges, resulting in opposite charges on the material's surfaces. Once the external force is removed, the material reverts to an uncharged state. Piezoelectric sensors exhibit high sensitivity and rapid response times to dynamic mechanical forces but show unreliability in static responses[43]

Among them, piezoresistive sensors are promising for diverse applications since they can be manufactured easily by low-cost fabrication techniques along with showing remarkable electrical properties, good sensitivity, mechanical stability, and fast response time. Thus, they find extensive use in fluid power systems that require precise electronic pressure measurements, wearable electronic devices for monitoring human motion, healthcare monitoring, flexible tactile sensing, and robotic devices [44–46]. To assess the performance of piezoresistive sensors, several parameters need to be considered, such as sensitivity, stability (the number of cycles the sensor can maintain its sensitivity), response time, linearity or nonlinearity, and recovery time [3].

Sensitivity refers to the relationship between the output signal and the initial output signal within a specific strain range. It is quantitatively measured by the gauge factor (GF). The GF can be defined in two ways: $(\Delta R/R_0)/\varepsilon$ or $(\Delta R/R_0)/P$, where ε represents the applied strain, $\Delta R/ R_0$ is the proportional change in resistivity, and P denotes the external pressure[47]. High sensitivity indicates a higher signal-to-noise ratio as well, enabling the sensor to detect subtle changes [48]. To effectively transduce signals,

a sensor needs to operate within a dynamic range, which is the range of strain (either stretching or compression) where the signal response is detectable [49]. It should be noted that a sensor may have multiple linear regimes with varying sensitivity values within the dynamic range. Response time and relaxation time are crucial parameters for assessing the speed at which a sensor can respond, which is important for applications such as evaluating pulse waveforms where the sensor needs to quickly detect each beat. Response time refers to the duration it takes for a sensor to reach its final signal amplitude when strain is applied, while relaxation time is the time it takes for the sensor to return to its original signal after the applied pressure is removed. It is worth noting that in cases where sensor response is rapid, the evaluation of these parameters is often limited by the equipment used to measure the sensor values. Consequently, reported response and relaxation times in literature may reflect equipment limitations rather than the intrinsic performance of the sensor [42]. Lastly, the detection limit is the minimum strain that a sensor can sense, and it is used to determine if a sensor can detect mechanical forces (stretch/pressure) suitable for a specific application.

The designing parameters for flexible tactile sensors working with the piezoresistivity mechanism would be discussed in detail as follows:

I. Sensitivity

The sensitivity or gauge factor (GF) plays a crucial role in tactile sensors, especially in ultrasensitive applications where it is essential for detecting subtle displacements or structural damage. In the realm of piezoresistive sensors, sensitivity is defined as the instantaneous ratio of the relative change in electrical resistance to the applied force (strain/pressure). The GF value exhibits significant variability due to different components, morphological structures, and processing techniques. Regarding E-CPnCs, the sensitivity is influenced by the materials type, dispersion, and morphology of fillers, as well as the interaction between nanomaterials and the polymer matrix. E-CPnCs with concentrations of conductive nanomaterials near the electrical percolation threshold typically show the most substantial variation in electrical resistance. However, operating very close to the percolation threshold can adversely impact device-to-device reproducibility[50,51]. Notably, improving sensitivity in E-CPnCs, often relying on the tunneling effect, involves increasing tunneling resistance or the proportion of tunneling resistance relative to the total resistance, rather than altering the total resistance itself [52]. In the case of microcellular structures, less material is required to reach the percolation threshold

compared to bulk composites. Moreover, the sandwich and gradient structures within microcellular structures may impact the sensitivity range.

II. Linearity

Linearity is defined as a proportional relationship between the electrical signal and the applied force which can be assessed through the coefficient of determination (R^2) in linear regression. A higher R^2 signifies a more robust linear relationship[53]. Generally, piezoresistive sensors tend to exhibit a nonlinear relationship, often attributed to microstructural changes as the sensing component shifts from a homogeneous to a heterogeneous morphology under mechanical forces. However, the formation of a robust network of conductive materials within the structure and strong bonding between materials and the matrix can contribute to a linear response[50].

The filler content is pivotal in determining the linearity behavior of E-CPnC based sensors. Near the percolation threshold, insufficient conductive particles prevent the creation of contact paths, leading to conductivity primarily through the tunneling effect. This results in exponential resistance growth, causing a nonlinear strain response. At concentrations well above the percolation threshold, resistance changes depend on structural variations in distinct strain domains. High-density, stable, and robust structures contribute to higher linearity, especially where conductivity becomes less influenced by smaller strains. In compressive sensors formed by microcellular structures, larger strains result in more connections between nanomaterials, potentially improving linearity. Therefore, observing a linear response in microcellular conductive composite sensors is more likely.

Substrate properties, as demonstrated by Yang et al.[54], can also influence linearity, with tuning ratios affecting Young's modulus and improving linearity in strain sensors based on graphene woven fabrics on PDMS. However, a trade-off relationship exists between high sensitivity and high linearity. Studies, such as the one by Benchirouf et al.[55], suggest that using hybrid sensing nanomaterials can improve both sensitivity and linearity in stretchable sensors. Overall, achieving a balance between high sensitivity, mechanical performance, and sufficient linearity remains a significant challenge in the development of piezoresistive sensors.

III. Durability and robustness

The robustness and reliability of tactile sensors become particularly crucial when exposed to dynamic forces. Therefore, hysteresis, response time, and dynamic durability are three essential parameters for

analyzing the sensor's performance. Hysteresis refers to the inconsistent or non-monotonic variation in piezoresistivity response, and it can be observed by examining the loading/unloading curves. Response time measures how quickly the strain sensor provides an accurate and stable signal in response to an applied force. Dynamic durability analyzes the long-term workability of sensors subjected to cyclic loading-unloading mechanical forces, focusing on maintaining a stable and reproducible resistive response as well as mechanical robustness. In general, the presence of hysteresis and response delay is a common phenomenon observed in all polymer-based tactile sensors. These phenomena are often attributed to the network breakdown and reformation during cyclic loading. The viscoelastic nature of polymers, viscoelastic characteristics of conductive nanomaterials, poor interfacial adhesion, and imperfect recovery of conduction paths due to friction between the solid-state sensing element and elastomeric molecules have impact on the reformation of a network. Therefore, establishing a robust network between elastomeric nanomaterials and the polymer matrix is crucial for minimizing hysteresis and facilitating a faster response. As a result, the percolation threshold, interactions, and the morphology of the network play a crucial role in these phenomena, which should be taken into consideration when selecting appropriate materials for fabricating microcellular sensors. It can be observed that networks with larger pores are more susceptible to damage during the application of mechanical forces [50].

IV. Detection limit

The detection limit represents the minimum quantity that a sensor can measure with a defined precision or reproducibility. For pressure tactile sensors, it is defined as the pressure at which the sensor can produce a reliable sensing response, denoted as the relative current or resistivity change ($\Delta I/I_0$ or $\Delta R/R_0$). Generally, the credibility of the detection limit requires sensing response ($\Delta I/I_0$ or $\Delta R/R_0$) to be sufficiently large from the noise, typically exceeding 10%. This ensures clear differentiation of the signal from the noise which caused by environmental disturbances or instrumental instability[56,57]. Detection limit of devices can be estimated by comparing the signal value to the baseline noise level. It's important to note that the detection limit can be defined as either three times the peak-to-peak noise or three times the root-mean-square (rms) noise. Therefore, the estimation of the signal-to-noise ratio of the sensor involves taking the sensing response of the sensor (after subtracting the background) and dividing it by the standard deviation of the response [58], as calculated by (Equation 2.5)[59]:

$$\boldsymbol{LOD} = \frac{\boldsymbol{3\sigma}}{\boldsymbol{S}} \qquad 2.5$$

where $\boldsymbol{\sigma}$ is the standard deviation of the response and $\boldsymbol{S}$ is the slope of calibration curve.

As an overview, taking into consideration the designing parameters for fabrication of piezoresistive sensors is crucial to enhance their performance. The use of conductive polymer nanocomposites has been recognized as a solution for designing piezoresistive sensors with acceptable performance and addressing the limitations of conventional piezoresistive sensors. Conventional sensors often suffer from issues such as rigidity, incompressibility, low GF, limited linear working range, slow response times, and response instability. By incorporating carbonaceous nanoparticles, the nanocomposites exhibit enhanced sensitivity due to the large surface area as well as high conductivity. By optimizing composition, structure, and processing parameters of polymer nanocomposites, it is possible to design sensors with enhanced performance to meet the specific requirements of different sensing applications.

2.3.2 Components of Flexible E-CPnCs

2.3.2.1 Polymer Matrix

Polymers are a group of materials that hold promise for the development of flexible electronic devices because of their excellent mechanical properties. Elastomers can withstand large strains and geometrical deformations, including bending, twisting, folding, and stretching. Various types of elastomeric matrices, including thermoplastics, thermosets, and hydrogels have been combined with conductive nanomaterials for fabrication of flexible and wearable electronic devices [60].

Thermosetting polymers are widely used in CPnCs due to their outstanding mechanical properties, chemical and thermal resistance resulting from crosslinks within the matrix. One such polymer is polydimethylsiloxane (PDMS), a silicon rubber with tunable Young's modulus ranging from 200 kPa to 3 GPa and high strain failure of up to 1000% [61,62]. PDMS has garnered significant attention in numerous flexible electronic devices, owing to its distinctive features. For instance, Nguyen et al. [63] fabricated multi-functional porous MXene/PDMS nanocomposite by utilizing Ni Foam as a template served as pressure piezoresistive sensors. The fabricated nanocomposite offered a sensitivity range of 0.02 kPa^{-1} to 0.12 kPa^{-1} due to the exceptional electrical conductivity, large specific surface area and impressive elasticity of observed characteristics.

Thermoplastic polymers are a class of easy-processable compounds that do not need additional crosslinker for curing reaction. Among these, thermoplastic polyurethane (TPU) and styrene-ethylene-

butylene-styrene (SEBS) are commonly used in the manufacturing of electronic devices [64,65]. Sun et al. [66] developed stretchable strain sensors by incorporating conductive silver flakes into two different elastomeric polymers, namely TPU and PDMS. The TPU-based nanocomposite was prepared by simply mixing conductive silver flakes into a TPU solution containing acetone and DMF. On the other hand, the processing of the PDMS nanocomposite involved planetary mixing and ball milling. The fabricated sensors exhibited a similar percolation threshold and achieved an electrical conductivity of 1000 S/cm. The researchers conducted a comparative analysis of the electrical and mechanical performance of both sensors. The sensitivity of the TPU sensor was approximately three times higher than that of PDMS, indicating that the sensitivity is influenced by the resistance gradient rather than the value of electrical conductivity alone. In terms of mechanical performance, the PDMS sensor demonstrated greater durability, withstanding up to 1000 cycles, due to the robust nature of thermoset polymers. This suggests that due to the weak non-covalent bonding within thermoplastic polymeric matrices, they may not be suitable for long-term mechanical testing, as well as for long-term thermal and chemical resistance applicability.

2.3.2.2 Conductive Nanomaterials

Various conductive nanomaterials can be utilized for designing multifunctional E-CPnCs, such as conductive metal nanowires/nanoparticles, carbon nanomaterials, liquid metals, conductive polymers, and their hybrids. These nanomaterials provide different electrical conductivity to E-CPnCs and determine the ultimate application. Among them, carbonaceous nanomaterials, including carbon nanotubes (CNTs), carbon nanofibers (CNFs), carbon blacks (CBs), and graphene have attracted significant attention due to their excellent electrical conductivity, outstanding mechanical fatigue resistance, good chemical/thermal stability, and relatively low cost [67,68].

Spherical carbonaceous nanofillers (0D) have been present since the 1900s, known as carbon black. It is the oldest allotrope of carbon which can be produced through pyrolysis with varying surface areas spanning from 20 to 500 m^2g^{-1}, and sizes ranging from 20 to 300 nm [69]. They have found widespread use as additives in commercially available conductive composites for energy-storage devices due to their exceptional mechanical strength, high electrical conductivity, excellent chemical stability, and relatively low cost. Zhai et al. [70]fabricated an aligned porous TPU/ CB nanocomposite using a unidirectional freeze-drying process. They observed two distinct linear regimes in the strain ranges of 0-66% and 66-82.57% with the GF value of 0.80 and 1.55 for regimes 1 and 2, respectively. They

suggested that the dual behavior was attributed to the minor evolution of the sponge frame and substantial deformation resulting from the air extrusion inside the pores under the low compressive strain. As the compressive strain increased, the remaining air in the pores decreased, and the sensing mechanism became more related to skeleton deformation.

One-dimensional carbonaceous nanofibers and nanotubes are promising candidates for fabricating stretchable conductors due to their remarkable electrical conductivity, high aspect ratio, and mechanical strength. Carbon nanotubes (CNTs) possess a lattice-like tubular structure with a high aspect ratio, consisting of a periodic honeycomb graphene network with carbon atoms covalently bonded. Generally, there are two types of carbon nanotubes: single-walled CNTs (SWCNTs) which consist of a single rolled graphene sheet, and multi-walled CNTs (MWCNTs) which involve multiple stacked graphitic shells forming a cylindrical tube. Compared to 0-D carbon blacks (CBs), 1-D CNTs are more effective as conductive fillers, enabling high electrical conductivity at relatively lower filler concentrations. By utilizing spray coated film of CNT on the elastomeric substrate, Lipomi et al [71] successfully produced a well-aligned CNT-based stretchable conductors with electrical conductivity of 2200 S/cm under 150% strain exhibiting excellent optical transparency. In contrast to CNTs, carbon nanofibers (CNFs) possess similar cylindrical nanostructures but have larger diameters and lengths, arranged in stacked cones, cups, or plates. The relatively less oriented nanostructure of CNFs results in more defects, leading to lower electrical and mechanical properties. Nevertheless, the lower cost of CNFs and their compromised yet still excellent electrical conductivity and mechanical strength make them suitable candidates for tough nanocomposites and soft strain sensors[72,73]. For instance, Wu et. al [74] fabricated a porous PDMS/CNF composite with 70% compressibility used for detecting human joints movement.

The use of 2D carbon nanosheets, including graphene and its derivatives, has gained significant attention in various fields due to their unique characteristics and exceptional properties. Graphene is renowned for its exceptional electrical properties, large surface area, excellent thermal conductivity, and impressive mechanical strength[75,76]. These properties make graphene highly desirable for applications in flexible electronics, energy storage devices, sensors, and composite materials. Additionally, three-dimensional porous conductive networks of graphene, such as graphene aerogels and graphene foams, featuring a large surface area and outstanding electrical conductivity, have been specifically designed to integrate with polymer matrices. This integration enables the development of flexible electronic devices[77,78]. For instance, Wu et al. [79] investigated the preparation of graphene

aerogel/PDMS nanocomposites with varying microstructures for use as piezoresistive sensors. Their findings revealed that nanocomposites with larger cell structures exhibited higher sensitivity, while those with thicker cell walls demonstrated lower sensitivity. Xu et al. [80] fabricated graphene/PDMS nanocomposites with a graphene loading of 3.07 wt %, with excellent electrical conductivity of 10^3 S/m and EMI SE of 54 dB in the X-band frequency range.

MXene is a relatively new class of two-dimensional transition metal carbides or nitrides that have gained significant attention in recent years. They are denoted as $M_{n+1}X_nT_x$, where M is an early transition metal such as Ti, Zr, V, Nb, Ta, or Mo and X is carbon and/or nitrogen. MXenes possess a unique structure consisting of stacked layers with highly conductive properties. They exhibit excellent electrical conductivity (reaching up to 10^6 S/m), good mechanical strength, and exceptional electrochemical performance, making them suitable for applications in energy storage devices, electromagnetic shielding, catalysis, and sensors[81]. Moreover, the surface functionalities naturally obtained through the acidic etching of the bulk MAX phase give rise to MXene's inherent hydrophilic nature, with functional groups such as a mixture of OH, O, and F as Tx, enabling its processability in aqueous solutions[82]. For instance, Zhao al. fabricated $Ti_3C_2T_x$ MXene/GO microcellular aerogel through freeze-casting method with excellent electrical conductivity of 696 S/m and EMI shielding effectiveness (SE) of 50 dB[83] . Lu et al. [84]successfully fabricated MXene based composite by using a double-network hydrogel consisting of polyvinyl alcohol (PVA) and polyvinylpyrrolidone (PVP) as the matrix. The 3D conductive network formed by MXene in the hydrogel showed high sensitivity and exceptional mechanical properties due to the robust interaction between MXene and the PVA/PVP hydrogel matrix. The fabricated sensor demonstrates outstanding performance, featuring high sensitivity (GF = 10.75), a short response time (33.5 ms), and a low detection limit of 0.87 Pa. These characteristics enable real-time and precise monitoring of human activities. Li et al. [85]employed a dipping and drying method to apply a coating of MXene on a PU sponge previously treated with chitosan to introduce a positive charge. Given that the $Ti_3C_2T_x$ sheet is negatively charged, the combination of the two materials is enhanced. The resulting sponge sensor exhibits a stable piezoresistive response, high compressibility, good structural stability, and a short response time (19 ms).

Graphene nanoribbons (GNRs) are narrow strips of graphene with quasi-one-dimensional structure that possess unique characteristics distinct from their two-dimensional graphene counterparts[86]. Jun et al.[87]investigated electrical and mechanical properties of TPU nanocomposites by incorporation GNR

and CNT. Their findings revealed that GNR/TPU nanocomposites exhibited higher electrical conductivity at lower percolation threshold, attributed to the enhanced filler-filler interfaces within the matrix. Additionally, the unzipping of CNTs resulted in a larger surface area along with edge structures of GNR nanocomposite. This modification significantly enhanced the filler-matrix interactions, leading to higher mechanical properties of GNR/TPU composites as well as increased EMI SE from 9.3 dB to 24.9 dB by only addition of 8.2 vol.% of GNR within TPU matrix. Lee et al. [88] fabricated a heterodimensional hybrid piezoresistive pressure sensor by incorporating 1D nitrogen doped GNR with 2D MXene sheets. The robust interaction between the MXene layers and the nitrogen functional groups within the composite enhanced sensing stability for up to 10,000 cycles at high pressures (100 kPa), demonstrating promising potential for smart seat cushion-based posture monitoring applications.

In summary, each conductive nanofiller possesses distinct physical properties, which are outlined in Table 2.1. The selection of the appropriate nanofiller should be based on the specific application requirements and desired properties.

Table 2.1 Physical properties of conductive nanofillers [89,90].

	Graphite	Carbon Black	Carbon nanotube	Graphene nanoribbon	Graphene nanoplatelets	MXene
Conductivity (S/cm)	400-1250	2.5-20	10^{-4}-10^{2}	10^{-4}-10^{2}	100-1000	4000-9000
Aspect ratio	Close to 1	Close to 1	1000-50000	1000-50000	10-1000	200-1600
Particle size (m)	6-200	0.014-0.25	L=10-100 D: few nm	L=10-100 W: few nm	5-200	1-10
Surface area (m^2/g)	6.2-20	7-560	200-250	250-500	20-150	19.6
Density (g/cm^3)	2-2.25	1.7-1.9	2	2	2-2.25	3.7

2.3.3 Fabrication Methods of Flexible E-CPnCs

In order to fabricate high-performance multifunctional E-CPnCs, the careful selection of appropriate processing methods is crucial. Several processing techniques have been developed, and they can be categorized based on the mechanical response of E-CPnCs into two main types: stretchable electronic devices and compressible ones. When it comes to designing stretchable electronic devices, common synthesis approaches such as melt blending, solution mixing, and in-situ polymerization are commonly employed. These methods are mostly based on integration of conductive nanofillers in the elastomeric polymer matrix with high yield of strain and stress. On the other hand, to produce compressible electronic devices, techniques like the sacrificial template method, freeze-casting, and foaming method are often utilized. It is important to note that there is no universal fabrication technique developed for design of all types of E-CPnCs. The selection of the most suitable processing methodology depends on several parameters, including the intended application area, availability of specific facilities, and processing efficiency. Moreover, the selection of the polymer and nanofillers is also influenced by the desired properties of the E-CPnCs, as polymers offer a wide range of physical and mechanical characteristics and nanofillers exhibit diverse electrical conductivity levels.

2.3.3.1 Fabrication of Stretchable E-CPnCs

Stretchable piezoresistive sensors are mainly fabricated through the common synthesis method for integration the conductive nanofiller within the flexible elastomer. For instance, solution mixing is a simple method wherein polymer and nanoparticles are combined in a suitable solvent and the solvent is subsequently evaporated. To ensure better dispersion of nanoparticles, mechanical stirring or ultrasonication is often employed. Although solution mixing is widely employed in scientific literature, the reliance on solvent evaporation limits its scalability for large-scale composite production. On the other hand, melt processing involves the blending of molten polymer with nanofillers. The highly viscous molten polymer generates significant shear forces, leading to the deagglomeration of nanoparticle aggregates or bundles and promoting dispersion. For instance, Jin et al.[91] utilized melt blending to incorporate varying loadings of MWCNTs into a polymethyl methacrylate (PMMA) matrix, investigating the dispersion and mechanical properties of the resulting composites. They reported well-dispersed nanotubes within the polymer matrix without observable damage to the nanotubes. Despite melt mixing is less efficient than solution mixing in terms of breaking nanoparticle aggregates, it is widely utilized in industrial practices due to the absence of solvent evaporation [92,93]. Additionally,

melt processing is suitable for polymers such as polyethylene and polypropylene, which are not soluble in common solvents.

2.3.3.2 Fabrication of Compressible E-CPnCs

Generally, compressive E-CPnCs are mainly fabricated through two-step processes that involve introducing air into the bulk nanocomposite to create a porous structure with compressibility and lightweight features. Researchers have developed several approaches for designing porous nanocomposites, which can be classified into four main methods, each with its own benefits and disadvantages. The first method involves using physical templates as sacrificial backbones, such as Ni foam, PU foam and sugar [94,95]. In this method, microcellular structures are created with the aid of a predefined template. Once the microcellular structure is formed, the template is then removed from the composite. While this method is simple, it lacks control over the structural design and requires harsh environmental conditions for template removal. For instance, Ni foam requires metal etching with a high concentration of HCl, and PU foam needs to be transformed into carbon through high temperature treatment up to 1000 ˚C in an inert atmosphere. In the case of sugar or glucose materials, the polymer matrix should be hydrophobic to resist the usage of water for template removal. For instance, Luo et al. [96] prepared Graphene/PDMS pressure sensor using Ni foam with a sensitivity of 15.9 kPa^{-1}, fast response time (1.2 ms) and high stability. The second approach involves dip coating of polymeric foams with a suspension of conductive nano fillers in a solvent. In this process, nanofillers dispersed in a proper solvent, and then polymeric foam is soaked in the filler suspension to coat nanofillers on the cell-walls of the pre-formed foam, followed by solvent evaporation[97]. Although this method is simple, the compatibility between the polymeric foam and the solvent should be considered since unproper choose of solvent results in swelling and deformability of the structure. Moreover, the weak physical bonding between the foam surface and fillers results in loose contact of conductive filler network and poor piezoresistive reversibility in sensors. Sengupta et al. [98] used a sugar scaffold PDMS foam to prepare graphene/PDMS sensor with two linear response regions with GF of 2.8 to 8.77 that could withstand 36000 cyclic compressive loading. Batch foaming is a low-cost and environmentally friendly method, but it involves a two-step fabrication process as well. In the first step, conductive nanomaterials are incorporated into polymer matrix using melt blending or solution mixing to produce a composite[99]. This process is followed by gas foaming using subcritical or supercritical CO_2 under specific conditions. However, this approach may sometimes present challenges in structural control, as fillers may form agglomerates, and the pore size is often uncontrollable due to difficulties

in control over CO_2 penetration[100]. Fei et al. [101] employed a multi-step method to produce a foam using supercritical CO_2. Initially, a cellulose/CNT network was created through freeze casting, followed by dipping in TPU to obtain a composite. Lastly, supercritical CO_2 was used to produce a compressive piezoresistive sensor with a high porosity of 90% and high conductivity of 2.04 $S.m^{-1}$. Freeze-casting method, as a processing technique for compressible E-CPnCs, introduces air into the mixture through subsequent sublimation of ice crystals in the freeze drier, resulting in creation of aligned structures. However, this method is not scalable and involves multiple steps, including freezing, sublimation, and dip coating of the polymer, especially when using hydrophobic elastomers, such as TPU or PDMS [102,103]. Huang et. al [104] prepared a graphene aerogel by using freeze casting method to produce a foam with high absorption energy that withstand 1000 cycles at 70% compressive strain. However, all the mentioned fabrication techniques for designing compressive E-CPnCs are complex, multi-step and costly. Therefore, it is essential to explore facile and one step fabrication methods to design 3D conductive structure of polymeric nanocomposites with excellent mechanical performance to serve as compressive piezoresistive sensor.

2.3.4 Multifunctional Microcellular E-CPnCs

In addition to microcellular-based tactile sensors, they have found diverse applications in electronic industry, energy storage devices and environment protection areas due to their exceptional properties, such as lightweightness, low density, tunable mechanical properties, high surface area and absorption efficiency, and superior EMI Shielding absorption efficiency.

2.3.4.1 Absorbent Materials

Regarding the environment protection, these materials can serve as absorbent materials. Their porosity, high surface area and hydrophobicity enable them to absorb organic solutions such as oil and organic contaminants from water. This feature holds significant potential for various industrial separation applications, ranging from mitigating environmental damage caused by oil spills to refining clean water. 3D microcellular CPnCs can demonstrate impressive recyclability through heating or squeezing. However, the process of heating poses notable complexities when dealing with solvents with high boiling points. Conversely, the squeezing method is typically applicable to elastic adsorbent materials. Since the brittle networks are susceptible to irreversible damage during mechanical deformations.

Consequently, there is a need to design and fabricate 3D microcellular materials with mechanical flexibility to serve as elastic adsorbent materials in the realm of oil–water separators[105].

2.3.4.2 Energy Storage Devices

In the electronics industry area, supercapacitors represent a category of electrochemical energy storage devices known for their high-power density, prolonged cycle life, and outstanding rate capability. These devices store charges either through ion adsorption at the electrode-electrolyte interface or rapid surface redox reactions. The utilization of microcellular E-CPnCs holds promise for their fabrication due to their interconnected pore structure. This type of network facilitates rapid ion and mass transfer, percolated electronic transport, low density, expansive surface area, and convenient access to surface adsorption sites[106,107].

2.3.4.3 EMI Shielding Materials

EMI shielding materials constitute a category of electrically conductive materials designed to protect against electromagnetic waves in the environment. Industries require these materials to not only possess effective EMI shielding properties but also to be lightweight and easy to process. Commercial EMI shielding materials should have shielding values of at least 20 dB and 30 dB to block 99% and 99.9% of incident electromagnetic waves, respectively[108]. The high electrical conductivity of the fillers in E-CPnCs enables them to effectively dissipate and reflect electromagnetic waves, providing efficient EMI shielding. Additionally, the lightweightness, chemical stability, easy processability and anti-corrosive properties of polymers make them valuable for EMI shielding applications. It is possible to tailor the EMI shielding properties of E-CPnCs, especially to meet absorbent-dominant shielding effectiveness by taking advantage of cellular networks.

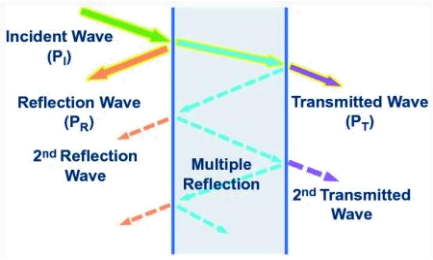


Figure 2.2. Schematic of shielding mechanisms by a shielding material[109].

Generally, materials attenuate electromagnetic waves through reflection (R), absorption (A), and multiple reflection (M). Therefore, the EMI Shielding Effectiveness (EMI SE) can be expressed as Equation 2.5 and depicted in Figure 2.2.

$$\boldsymbol{EMI\ SE = R + A + M} \quad 2.5$$

The reflection mechanism is the reflection of a proportion of the incident EM waves from the surface of the shielding material which is due to the abundant free surface charge carriers at the surface of the shielding material [110]. However, the absorption mechanism is a proportion of the transmitted EM wave within the shield that is dissipated by absorption and turning to heat [111]. The internal multiple reflection mechanism refers to the phenomenon where electromagnetic waves that have already been reflected within an EMI shielding material undergo further reflections [112]. Amplifying the absorption shielding mechanism of EMI shielding material is crucial because relying solely on a reflective shielding mechanism can cause secondary EMI pollution when the reflected EM waves interact with other devices. Therefore, there have been recent efforts to enhance EMI SE by tuning nanocomposites to exhibit absorptive dominant shielding behavior.

2.4 Conclusions and Future Perspectives

In conclusion, the fabrication of E-CPnCs for advanced tactile sensors does not rely on a universal technique. Specific requirements must be taken into account to ensure the functionality of physical sensors. This can be achieved by designing E-CPnCs through a combination of material control and process control methodologies. For instance, for compressive sensors, both electrical conductivity and mechanical performance should be considered to achieve high sensitivity and durability. It should be noted that controlling the microstructure enhances the functionality of sensors, allowing for a broader detection range, higher gauge factor, and improved attenuation of EM waves within the structure for multifunctional devices. These objectives can be accomplished through specific fabrication processes. As a result, this research is based on an in-depth investigation of a novel processing control for fabrication of E-CPnCs, which are extensively described in chapter 4.

Chapter 3
Characterization Techniques

In order to characterize conductive polymer nanocomposites, this chapter briefly describes several employed techniques.

3.1 X-ray Diffraction (XRD)

X-ray diffraction (XRD) is a powerful non-destructive method used to identify atomic and molecular structure of crystalline materials. It works based on the ability of the crystal's interaction with the X-ray beam, in which the atoms in the crystal lattice cause diffraction of the incident X-ray beam in different directions. The X-ray source is swept over a range of angles and the diffracted x-rays at specific angles are collected and processed by the detector. Crystal structure, orientation and the spacing between atoms could be analyzed by the angle and intensities of diffracted beams. The crystal orientation and spacing could be correlated to the diffraction angle with Bragg's law (Equation 3.1) expressed as below:

$$2d \sin\theta = n\lambda \tag{3.1}$$

where n, λ, d, and θ represent the order of the spectrum (an integer), the wavelength of the X-rays (λ=1.5418 Å for Cu K_α), the spacing between diffracting planes, and the incident angle, respectively.

Besides, the crystal size and the morphology of crystalline material can be determined by Scherrer equation (Equation 3.2) as follows. In this formula, τ represents the crystal size and β is the full width at half maximum (FWHM) intensity of the peak at 2θ diffraction angle.

$$\tau = \frac{0.89\lambda}{\beta \cos(\theta)} \tag{3.2}$$

Moreover, the average number of layers (L_x) can also be calculated by dividing the crystal size over interlayer distance ($L_x = \frac{\tau}{d}$).

3.2 Raman Spectroscopy

Raman spectroscopy is a non-destructive analytical technique based on the vibration of atoms in the molecule by interacting with monochromatic light. In this technique, a laser beam with unique wavelength is directed on the sample, and the scattered light with different wavelengths is collected by a spectrometer. The shift in the wavelengths is called Raman shift that depends on the vibrational and rotational modes of molecules. As each chemical compound has unique Raman spectrum, this method can be used to identify unknown substances and also monitor chemical reactions in real time by providing information about chemical composition and molecular structures.

Raman spectroscopy is a fast, powerful, and highly sensitive method to characterize carbonaceous materials. It could provide information about the disorder's degree and sp^2 hybridization of carbon atoms. The Raman spectrum of carbonaceous materials is dominated by two major peaks, known as D band and G band. The D band is located at the frequency of 1350 cm^{-1} and as an indicator of disorder and defects in the material. The higher number of defects leads to a stronger D band. The G-band arises from the vibration of sp^2-hybridized carbon atoms in graphitic domains, and its position and width provide information about the degree of graphitization or the extent of the crystalline structure in the material. Generally, a higher intensity and narrower width of the G-band indicates a higher degree of graphitization.

3.3 X-ray photoelectron spectroscopy (XPS)

X-ray Photoelectron Spectroscopy (XPS) is a surface-sensitive analytical method, providing detailed information about the elemental composition and chemical states of materials. XPS is particularly advantageous for studying the surface composition of thin films, nanomaterials, and interfaces. Utilizing X-ray irradiation, the technique induces photoelectron emission from the sample's surface, and the resulting energy distribution of emitted electrons is analyzed. This process enables precise identification of elements present in the material, along with information about their chemical bonding environments. XPS spectra offer detailed peaks corresponding to the binding energies of electrons emitted from various elements, enabling precise identification of the elements present in the sample. Moreover, the spectral lines' intensity provides quantitative information about the elemental composition, offering insights into the material's stoichiometry. Furthermore, XPS provides valuable data on the chemical state of elements, showing their bonding environments and oxidation states.

3.4 Scanning Electron Microscopy (SEM)

Scanning Electron Microscopy (SEM) is a high-resolution imaging technique that utilizes a focused beam of electrons to investigate the surface morphology, topography, and composition of micro and nanoscale samples with excellent spatial resolution. In this technique, a sample is placed in a high vacuum chamber, and a beam of electrons is directed towards the sample surface, causing the emission of various signals such as secondary electrons, backscattered electrons, and X-rays. Secondary electrons are low-energy electrons that are emitted from the surface of the sample when the primary electron beam interacts with the atoms on the surface. These electrons carry information about the surface topography and morphology of the sample and can be used to generate high-resolution images of the sample surface. Backscattered electrons, on the other hand, are higher energy electrons that are scattered back from the sample due to interactions with the atomic nuclei of the sample. These electrons provide information about the sample's composition and can be used to generate images that reveal the sample's elemental composition and density variations. Moreover, the energy and intensity of X-rays could be analyzed by an energy-dispersive X-ray spectrometer (EDX) detector. Thus, EDX is a technique that can be used in conjugation with SEM to provide information about different element composition and their distribution within the sample.

3.5 Mechanical Properties

The mechanical properties of materials can be analyzed using Universal Testing Machine (UTM) in different testing modes, including tensile and compression modes. In tensile testing, the sample is clamped between two grips and elongated at a constant rate to the point where it breaks. During the test, the elongation or deformation of the sample is recorded, and the resulting strain-stress curve is generated. On the other hand, in compression testing, the sample is placed between two planar surfaces and compressed at a constant rate until it fails. By analyzing the strain-stress curve of materials, various properties such as Young’s modulus, tensile/compressive strength, and elongation/compressive strain at break can be calculated. Young’s modulus represents the stiffness of a material measured as the initial slope of the strain-stress curve. Tensile or compressive strength is a measurement of the force required to pull/press a material to the point where it breaks. It is the maximum value of stress that the material can withstand before failure. Meanwhile, maximum strain of a material before failure is presented as elongation/ compressive strain at break.

Furthermore, cyclic testing can also be performed in compression mode to analyze hysteresis curves of loading-unloading cycles. It represents the material's shape memory performance and the material's ability to recover to its initial state. By performing numerous cycles on the material, its fatigue resistance can also be investigated.

3.6 Electrochemical Analysis

Electrochemical testing is a powerful analytical tool used to study the behavior of electrochemical systems. There are several techniques used for material analysis from simple potentiostat methods like chronoamperometry (CA) to potentiodynamic methods such as cyclic voltammetry (CV) and complex AC techniques, known as electrochemical impedance spectroscopy (EIS).

Chronoamperometry (CA) is an electrochemical technique used to measure the current response of an electrode over time in response to a constant applied potential. While, in cyclic voltammetry (CV) the current is measured as a function of the applied potential, where the potential is swept in a cyclic manner between two values. In both methods, a sample is placed in an electrochemical cell, and potential is applied to the working electrode. CA technique provides information about the electrochemical properties of the sample by analyzing the current response as a function of constant potential. However, the CV technique provides valuable information about the kinetics and thermodynamics of electrochemical reactions by analyzing current response against varied potential.

Electrochemical impedance spectroscopy (EIS) is an electrochemical technique that measures the impedance of a material over a range of frequencies. During an EIS experiment, a small amplitude alternating current is applied to the sample at different frequencies, and the resulting voltage is measured. The impedance of the sample is then calculated by dividing the voltage by the current. This technique can provide information about the electrical properties of a material, such as resistance, capacitance, and inductance, and can be used to study electrochemical processes.

3.7 Electrical Conductivity and Dielectric Properties Measurement

There are several techniques used to measure dielectric properties of materials, each with their own advantages and limitations. The choice of measurement technique depends on several factors such as

the nature of material, size, shape, and the frequency range of interest, as well as the availability of instrumentations. For instance, the capacitance measurement technique involves creating a capacitor using the material of interest and then measuring the charge stored on it by analyzing the voltage and current passing through of this capacitor. This technique is relatively simple and inexpensive and can be used to measure dielectric constants in a wide range of materials. However, it is limited by the requirement for a parallel-plate capacitor geometry, and the presence of conductive filler particles in the material can affect the measurement. Impedance spectroscopy is another technique which measures the material's response to an alternating electric field of varying frequencies, allowing for the determination of the dielectric constant and loss as a function of frequency. This non-invasive technique can provide information about the frequency dependence of dielectric properties. However, it is a more complex method and requires specialized equipment. Another method, known as dielectric relaxation spectroscopy (DRS), measures the relaxation behavior of the material under an electric field, allowing for the determination of the relaxation time and activation energy of the material. This technique can provide information about the molecular structure and dynamics of the material and is particularly useful for studying polymers and other complex materials. However, it requires careful control of temperature and frequency and is generally more time-consuming and expensive than other techniques.

3.8 Thermal Conductivity Measurement

Thermal conductivity is a crucial property that describes a material's ability to conduct heat. This property is measured as the rate at which heat is transferred through a material when there is a temperature difference across it. To determine the thermal conductivity of a material, several methods have been developed, including steady-state and unsteady-state conditions.

In the steady-state condition, a constant heat flux is applied to one side of the material, and the temperature difference between the two sides of the material is measured. On the other hand, in the unsteady-state condition, the heat flux or temperature difference is not constant, and the temperature response of the material is measured over time. The selection of the measurement method depends on various factors, such as the size, shape, type of material, and the required accuracy for the application. For example, the transient method measures the temperature change of a material over time after a heat pulse is applied to it. This method is commonly used for materials with low thermal conductivities, such as insulators. The guarded hot plate method involves sandwiching the material between two plates

that are kept at different temperatures, while measuring the temperature difference and heat flow through the material. The laser flash method, on the other hand, uses a high-intensity laser pulse to heat a small portion of the material, while measuring the temperature rise and the time it takes for the heat to spread through the material. This method is particularly useful for measuring the thermal conductivity of thin films and small samples.

3.9 Electromechanical Characterization

Electromechanical testing is used to accurately measure the sensor's response to mechanical deformation. The measurement process involves subjecting the sensor to controlled mechanical stress or strain while simultaneously monitoring the corresponding electrical output. This is achieved by mounting the sensor onto a testing setup that enables precise application of mechanical forces or strains such as universal testing machine. To capture the electrical output, the sensor is connected to a data acquisition system that records the changes in the electrical properties in response to the applied mechanical stimuli. The recorded data is then analyzed to determine the sensor's electromechanical performance and characteristics such as sensitivity, linearity, and dynamic range of the sensor. By analyzing the electrical output in relation to the applied mechanical stress or strain, known as gauge factor, valuable insights can be gained regarding the sensor's functionality and its suitability for specific applications, such as health monitoring, robotics, biomechanics, and industrial process control.

Gauge factor can be expressed through the formula for the piezoresistive sensors (Equation 3.3):

$$\boldsymbol{GF} = \frac{\boldsymbol{R-R_0}}{\boldsymbol{\varepsilon R_0}} = \frac{\boldsymbol{\Delta R}}{\boldsymbol{\varepsilon R_0}} \tag{3.3}$$

where R represents the resistance of the sensors when subjected to a compressive/tensile strain of ε, and R_0 denotes the initial resistance of the sensors.

Chapter 4

Fabrication of Cellular Electrically Conductive Graphene-PDMS based Composite through Novel One-pot Synthesis

4.1 Introduction

In recent years, tactile physical sensors have become integral to our lives, simplifying tasks and enhancing comfort. These sensors find extensive use in healthcare, human motion detection, and Human-Machine Interfaces (HMI). The flexibility and robustness of sensors offer significant advantages in accommodating both low and high strain levels. Traditional metal sensors and inorganic semiconductor materials encounter limitations in applications requiring extensive deformation or close integration with irregular surfaces due to their inherent brittleness, rigidity, low sensitivity, limited fatigue life, environmental sensitivity, and poor biocompatibility. Addressing these challenges, sensors based on E-CPnC have been developed in recent decades to create compressive and stretchable sensors.

Compressive sensors are particularly useful in scenarios where pressure control is essential, such as posture recognition, tapping, joint movements in human health monitoring, or managing pressure flow in automations. However, fabricating compressive sensors necessitates the formation of microcellular structures, where pores provide compressibility. Current methods for producing these structures involve complex and multi-step processes, highlighting the emerging need for a simplified and one-step approach. In this project, we introduce a straightforward method to fabricate a graphene-PDMS-based nanocomposite for piezoresistive sensing applications using the soft-templating method. Taking advantage of the physical properties of cyclohexane, this method is designed to create a microcellular structure through the rapid evaporation of cyclohexane, followed by the crosslinking of thermoset PDMS to form a 3D network.

4.2 Experimental Section

4.2.1 Materials and chemicals:

Graphite (2-15 μm diameter) was purchased from the Alfa-Aesar. Sulfuric acid (H_2SO_4, >99%), phosphoric acid (H_3PO_4, >99%), hydrogen peroxide (H_2O_2, 30%), hydrogen chloride (HCl, 37%), and potassium permanganate ($KMnO_4$) were supplied from Sigma Aldrich. PDMS (Sylgard 184 kit)

containing base polymer and curing agent with 10:1 mass ratio as an elastic component in this study was acquired from Dow Chemical co. All chemicals were used without further purification.

4.2.2 Synthesis of conductive graphene

In this study, Graphene oxide (GO) was prepared using an improved Hummer's method[113] as shown in Figure 4.1. 2 g graphite was dispersed in 360 ml H_2SO_4 in an ice bath while stirring for 1 hour. Followed by stirring for an additional 15 minutes after adding 40 ml of H_3PO_4. In the next step, 18 g oxidizing agent ($KMnO_4$) was gradually added at intervals of 2 minutes, with 1 g of $KMnO_4$ added each time. Subsequently, the solution was stirred for another 15 minutes until the color of mixture changed from black to dark green. Afterward, the oil bath was substituted by the ice bath and the temperature of the dispersion was raised to 50 ˚C and kept at this temperature for 16 hours. After which, the mixture was cooled down to the temperature of 0-4 ˚C by keeping in the ice bath. At this stage, 20 ml of H_2O_2 diluted in 400 ml of Deionized (DI) water was gradually added to the mixture until the color changed to yellowish brown. Finally, the resulting GO solution was washed with hydrochloric acid, ethanol, and water to reach a pH of 5.5-6.5. Then, the solution was freeze-dried for 3 days to obtain exfoliated GO powder.

Finally, a thermal shock method was employed to achieve a reduced form of the oxidized material. Thermal reduction is a cost effective, environmentally friendly, and large-scale process for reducing nanomaterials compared to the chemical reduction method[114]. Therefore, reduced graphene oxide (rGO) was obtained by subjecting their oxidated counterparts to quick thermal shock treatment at 900 °C under an inert Ar environment.

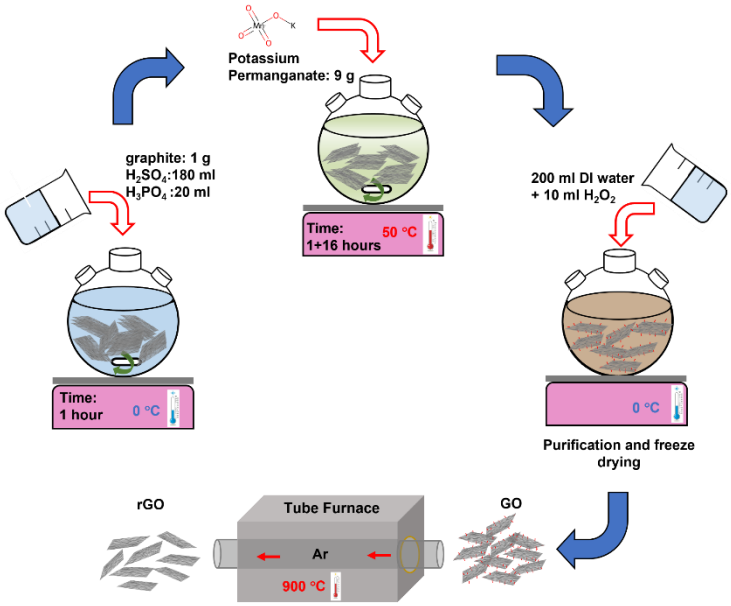


Figure 4.1 Schematic illustration of graphene production process.

4.2.3 Fabrication of 3D porous graphene-PDMS foam:

In this study, a facile and one-pot method was used for foam fabrication, based on the rapid evaporation of cyclohexane as shown Figure 4.2. To produce foams with varying porosity, foams were created using 60 mg of dispersed graphene in different concentrations of cyclohexane. The volume percent (V_c) of nanomaterials in the composite was calculated using the following formula (Equation 4.1) [115]:

$$\boldsymbol{V_c = \rho_f \times W_c/\rho_c} \qquad 4.1$$

where Wc is the weight fraction of nanomaterial in the composite. ρ_f and ρ_c are the density of the G-PDMS foam and the true density of the graphene which is 2.2 g/cm^3[116], respectively. The density of the porous G-PDMS microcellular structures was determined using the water displacement method. This involved measuring the weight of the foams both in the air and while submerged in water. Subsequently, the density of the foams was calculated using equation 4.2. To ensure better dispersion of graphene in the cyclohexane, the dispersion was mixed using the planetary centrifugal mixer (PCM, Thinky AR-100) for 30 minutes, followed by sonication for 3 hours. Subsequently, 1040 mg PDMS base polymer with 104 mg PDMS curing agent was added to the dispersion (to achieve 5 weight percent of graphene in the graphene-PDMS composite). The mixture was again mixed by PCM for 30 minutes, accompanied by sonication for an hour to enhance better dispersion and distribution of graphene in the

mixture. Afterward, the mixture was poured into the molds and frozen in liquid nitrogen for 5 minutes. Finally, freeze-dried in the freeze drier at 50 μbar for 3 hours, followed by curing in an oven at 80 ˚C overnight. The obtained foams were denoted as G-PDMSx, where x is the volume percent of graphene in G-PDMS porous structure, summarized in Table 4.1.

Table 4.1 Physical properties of G-PDMS foams.

Sample	G-PDMS43	G-PDMS48	G-PDMS70	G-PDMS77	G-PDMS87
Graphene Volume Percent (Vol.%)	0.429	0.481	0.700	0.772	0.872
Foam Density (g/cm^3)	0.189	0.212	0.308	0.34	0.384
Foam Void Fraction (%)	82.6	80.5	71.7	68.8	64.8

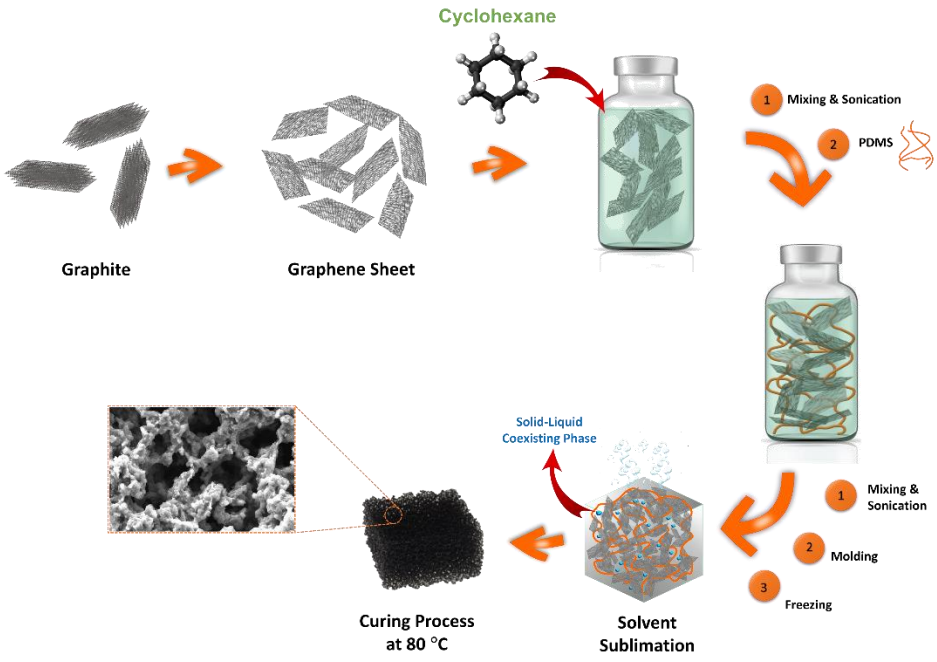


Figure 4.2 Schematic illustration of 3D microcellular graphene-PDMS preparation process.

4.3 Characterization

4.3.1 Morphology and physiochemical analysis of nanomaterials

The crystallographic pattern of conductive nanomaterials was recorded using an X-ray diffraction analyzer (XRD, Rigaku Miniflex 600) with a Cu Kα radiation source (λ = 1.54184 Å). Raman spectroscopy (Bruker SENTERRA, laser source of 20mW He-Ne at 532 nm) was used for analyzing structural integrity, defects, and structure disorders of nanomaterials. For analyzing the morphological properties of nanomaterials and the 3D structure of foams, field emission scanning electron microscopy (FESEM, Zeiss UltraPlus) was used. To analyze the elemental compositions and chemical states of nanomaterials, X-ray photoelectron spectroscopy (XPS, Thermal Scientific KAlpha) was used.

4.3.2 Characterization, electrical and mechanical performance of fabricated sensors

Various characterization techniques were used to investigate the properties and performance of the 3D porous network sensors as follows:

The microcellular structures were analyzed using FESEM (Zeiss UltraPlus) for investigating the morphological aspect of the sensors. The density of the foams was measured using water displacement method by a home-made device according to the ASTM D792-00, shown in Figure 4.3. In this method, the weight of the foams was measured in air and in water, and the density was calculated using Equation 4.2.

$$\boldsymbol{\rho_f = \frac{m_a}{m_a - m_w} \times \rho_w} \qquad 4.2$$

where ρ_f and ρ_w are the density of the foam and water, respectively. m_a and m_w are the weight of the foam measured in the air and while completely immersed in the water, correspondingly. Additionally, void fraction can be calculated by density of the foam (ρ_f) and bulk density (ρ_b) of the composite (unfoamed compound) with the Equation 4.3[117].

$$\boldsymbol{VF = 1 - \rho_f / \rho_b} \qquad 4.3$$

For the electrical properties of the sensors, measurements were taken using the Biologic potentiostat (Biologic VSP-300). The AC conductivity and dielectric properties were analyzed by the electrochemical impedance spectroscopy (EIS) method over a frequency sweep ranging from 0.01 Hz to 1 MHz. Additionally, the DC conductivity and resistance were analyzed through linear sweep

voltammetry (LSV) testing by the voltage ranging from -10V to 10V. All testing was performed using a four-point probe through-plane testing method.

The mechanical properties of sensors were studied by the universal testing machine (UTM, CellScale, UniVert) in compression mode. The compression test speed rate was set to 1 mm.min^{-1} for mechanical performance testing (usual stress-strain testing), and it was set to 3 mm.min^{-1} for investigating the fatigue cyclic testing. The compressive stress-strain hysteresis curves, mechanical strength, Young's modules, maximum compressive strain were obtained by the loading/unloading force-distance curves. A total of 500 cyclic compression/recovery testing was performed for investigating the fatigue resistance of the best sensor samples at 30% compressive strain. The energy loss coefficient and stress retention were calculated at 1, 10, 50, 150, 250, 500 cycles. Stress retention is defined by the maximum compression strength of sensors at each cycle. Additionally, the energy loss coefficient (ψ) was calculated using Equation 4.4.

$$\boldsymbol{\psi} = \frac{\boldsymbol{U_c - U_r}}{\boldsymbol{U_c}} = \frac{\boldsymbol{\Delta U}}{\boldsymbol{U_c}} \tag{4.4}$$

where U_c and U_r are the work of compression and recovery of stress-strain curves, respectively, which were calculated by integration of the loading and unloading curves by MATLAB.

To evaluate the sensing performance, a universal testing machine coupled with an electrochemical workstation as a data acquisition device were used. In this set up, the electrodes were connected to the data acquisition device using contact alligator clips, and the sensors were integrated into electrode system, in which two copper plates were attached to either end of each sensor via silver paste and conductive carbon tapes. The sensitivity of the sensors was evaluated by determining the strain gauge factor (GF) from the I-V curves. The corresponding GF for each sensor at their respective compressive strains was calculated using Equation 4.5.

$$\boldsymbol{GF} = \frac{\boldsymbol{R - R_0}}{\boldsymbol{\varepsilon R_0}} = \frac{\boldsymbol{\Delta R}}{\boldsymbol{\varepsilon R_0}} \tag{4.5}$$

where R represents the resistance of the foams when subjected to a compressive strain of ε, while R_0 denotes the initial resistance of the foams.

To assess the performance of the fabricated sensors in real-world scenarios, a tapping test was conducted to evaluate their sensitivity response to pressure and vibration, and human motion was monitored using the sensors to determine their accuracy and reliability in detecting movement. The

tapping test was performed on the pressure sensors to assess their consistency and repeatability in detecting pressure changes. During tapping test, the frequency and amplitude of the tapping were varied to determine the sensor's response.

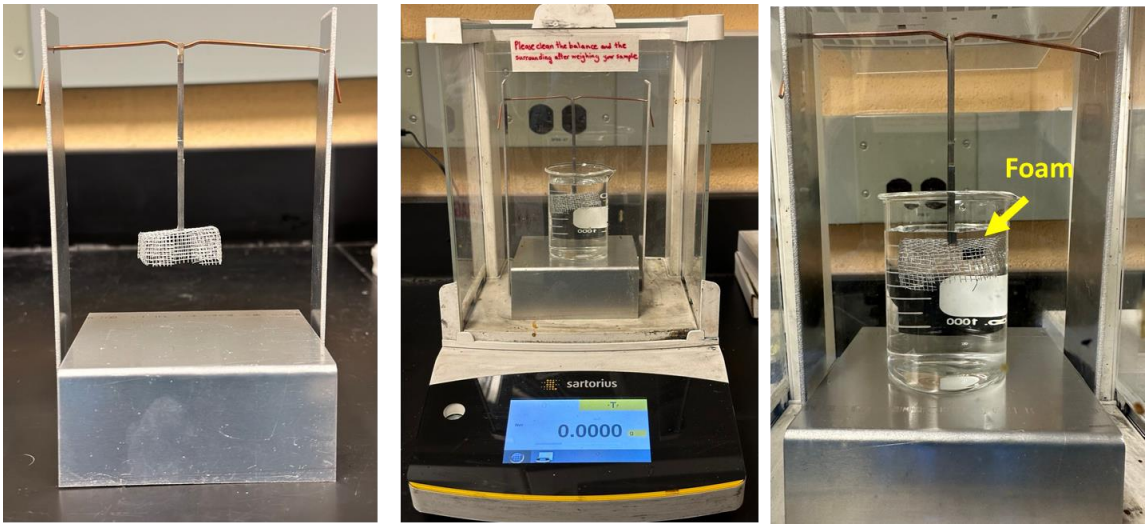


Figure 4.3 Home-made density measurement apparatus.

4.4 Results and Discussion

4.4.1 Nanomaterials characterization

Figure 4.4a depicts the crystallographic spectra of the nanomaterials along with the corresponding parameters have been extracted and presented in Table 4.2. Graphite showed a graphitic crystalline structure, with nearly identical 2θ angles of 26.76°. Chemical oxidation of graphite shifted the characteristics peaks to lower 2θ of 10.5°, for GO, indicating an increase in d-spacing. The increase in interlayer distance is attributed to the intercalation of oxygen containing functional groups, such as carboxyl, hydroxyl and epoxide groups on the edges and surfaces of the graphitic structures [118]. After employing thermal shock reduction at 900°C, the oxidation-induced characteristic peaks in graphene sheets disappeared, and a broad peak at about 25-26° emerged. This is due to the elimination of functional groups and reconstruction of sp^2 structures on graphitic layers. Furthermore, delamination of the graphene sheets to mono or few layers decreased the intensity of the characteristic peaks.

The chemical fingerprints of the graphene nanomaterials were explored through Raman spectroscopy, as presented in Figure 4.4b and the corresponding parameters extracted and summarized in Table 4.2. All nanomaterials showed three characteristic peaks associated with the D, G, and 2D modes at 1335 cm^{-1}, 1580 cm^{-1}, and 2680 cm^{-1}, respectively [119]. The D mode is related to the defects and disorders of the graphitic structure and is activated in the vicinity of structural imperfections, while the G mode results from the first-order scattering of E_{2g} mode. This mode is associated with in-plane optical phonon vibrations, which involve the stretching or compression of C-C bonds within the graphene lattice. The intensity ratio of D band over G band (I_D/I_G) was calculated to quantify the structural integrity of the graphene sheets. Graphite showed a very low I_D/I_G ratio 0.09, indicating the highest structural integrity and the least number of defects. However, introduction of oxygen containing functional groups on the edge and surface of the graphene sheet turned the sp^2 structure of graphene to sp^3 and thus significantly increased the ratio to 1.07. Thermal shock reduction of graphene oxide slightly reduced I_D/I_G ratio to 1.02, which is due to restoration of the graphene sp^2 structures. The edge structures act as disorders in graphitic structure and intensify the D band in Raman spectrum. The increase of the I_D/I_G ratio after thermal reduction was also explained by a reduction in the size of the restored sp^2.

The surface chemistry of the synthesized graphene sheets, before and after thermal shock reduction, was thoroughly explored by X-ray photoelectron spectroscopy (XPS) and described in Figure 4.4c-d. The C1s XPS spectra of GO revealed four distinctive peaks corresponding to carbon atoms in various oxygen containing functional groups: non-functionalized C=C ring at 284.6 eV, carbon in C-C band at 285.5 eV, C=O band at 286.1 eV, and O-C=O band at 290 eV. These peaks are indicative of the extensive oxidation state of graphene sheets [120]. The successful thermal shock reduction of graphene sheets was also confirmed by comparing XPS spectra in Figure 4.4c with their reduced counterparts in Figure 4.4d. Upon thermal shock reduction, the intensity of three latter peaks diminished, while the non-functionalized C=C ring band at 284.6 eV significantly intensified. This confirms the restoration of sp^2 carbon configurations by elimination of the functional groups.

Figure 4.4e-h present SEM images of graphite and graphene sheets after thermal shock reduction. The stacked layers of graphene sheets in SEM images of graphite in Figure 4.4e-f is obvious, while the crumbled paper-like morphology of the graphene sheets in Figure 4.4g-h indicates successful exfoliation of the graphene layers.

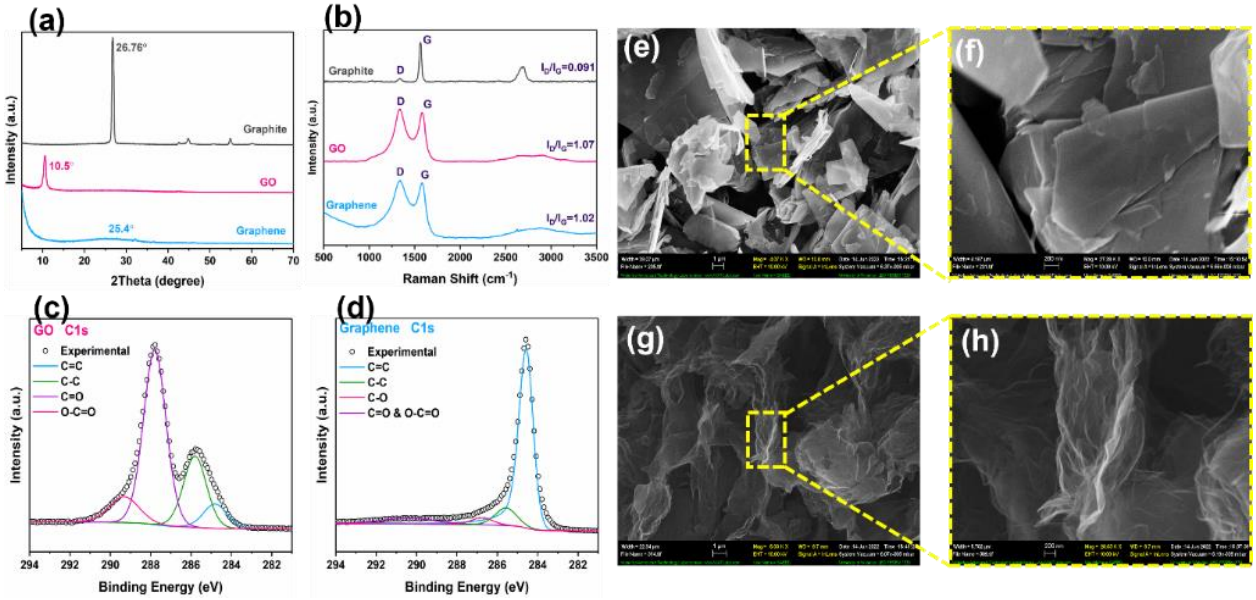


Figure 4.4 (a) XRD graphs (b) Raman Spectra (c-d) C1s high resolution XPS of GO and graphene sheets, and SEM images of (e-f) graphite and (g-h) graphene.

Table 4.2 Extracted parameters from the XRD and Raman graph.

	XRD					Raman
Nanomaterials	**2Θ (degree)**	**Interlayer Distance (Å)**	**FWHM (radian)**	**τ (Å)**	**Number of layers (L_x)**	I_D/I_G
Graphite	26.76	3.330	0.00905	155.803	46.780	0.090
GO	10.5	8.423	0.01201	114.719	13.619	1.070
Graphene	25.40	3.506	0.25865	5.438	1.551	1.027

4.4.2 Characterization of G-PDMS foams

The morphological structures of G-PDMS foams generated through a rapid solvent evaporation process with varying amounts of cyclohexane were analyzed using SEM. As displayed in Figure 4.5, the 3D porous structure of foams is induced by formation of soft template of cyclohexane crystals within the composite [121]. When a vacuum is applied in the freeze dryer, cyclohexane rapidly evaporates in an endothermic process, leading to heat loss throughout the mixture. Under controlled pressure and obtained temperature conditions, the cyclohexene triple point is reached, leading to a phase transition from liquid to a coexistence of liquid and ice phase. The formation of soft template composed of cyclohexane's crystals occupy some spaces within the mixture depending on the solvent concentration.

Consequently, as the mixture undergoes evaporation, this pore template facilitates the transformation of bulk structure into a porous one [122]. During the fabrication process, as cyclohexane evaporates and PDMS undergoes complete crosslinking, a stochastic interconnected cellular structure is formed where the graphene sheets are completely wrapped with PDMS via Van der Waals interactions. The presence of PDMS agglomerates in the foam structure can be attributed to the low volume percentage of graphene in the composite (with a weight ratio of graphene to PDMS of 1:19). As can be depicted from the SEM images, an increase in the solvent content leads to significant changes in the pore size and distribution.

Figure 4.5a1-a2 depict the intact network structure of G-PDMS87, featuring a small number of pores that are also small in size, with mainly maximum size of 10 micrometers. In contrast, G-PDMS43 exhibits a higher occurrence of larger pores with a broad size distribution ranging from 10 to 50 micrometers, as illustrated in Figure 4.5 c1-c2. The lower thickness of cell-walls observed in these figures can be attributed to the low amount of graphene present in the unit volume of G-PDMS43. The cellular structure of G-PDMS70 is presented in Figure 4.5 b1-b2, highlighting a relatively organized cellular arrangement when compared to G-PDMS87. Additionally, it exhibits a lower degree of porosity in comparison to the G-PDMS43 cellular structure. To acquire quantitative data, foam's density and void fraction were calculated based on the formula described in the experimental section and reported in Table 4.3. The findings indicate a direct relationship between the solvent content in the composite and the porosity and void fraction, with higher solvent content leading to increased porosity and void fraction, and a subsequent decrease in density.

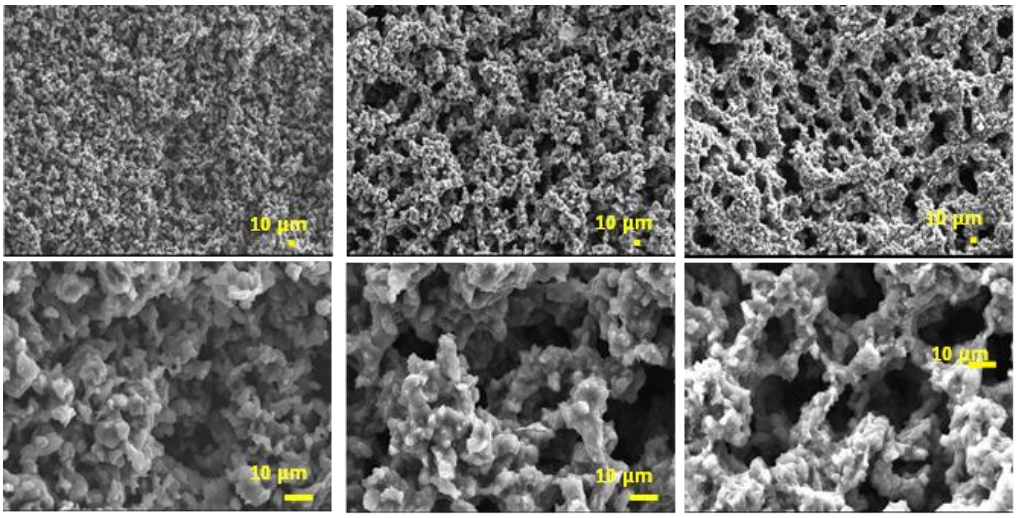


Figure 4.5 SEM images of G-PDMS foams, (a1-a2) SEM images of G-PDMS87 with 250X and 1000X magnification, (b1-b2) SEM images of G-PDMS70 with 250X and 1000X magnification, (c1-c2) SEM images of G-PDMS43 with 250X and 1000X magnification.

Table 4.3 Physical properties of G-PDMS foams.

Sample	G-PDMS43	G-PDMS48	G-PDMS70	G-PDMS77	G-PDMS87
Graphene Volume Percent (Vol.%)	0.429	0.481	0.700	0.772	0.872
Foam Density (g/cm^3)	0.189	0.212	0.308	0.34	0.384
Foam Void Fraction (%)	82.6	80.5	71.7	68.8	64.8

4.4.3 Electrical Conductivity of G-PDMS sensors.

The electrical and electromechanical properties of the microcellular G-PDMS foams were evaluated, as shown in Figure 4.6**.** Figure 4.6a**.** demonstrates the broadband Alternating Current (AC) conductivity as a function of frequency within the range of 0.1 Hz to 1 MHz. It can be observed that the AC conductivity of all porous nanocomposites exhibited a frequency independent behavior, which is a

characteristic of conductive nanocomposites above their percolation threshold. When the percolation threshold is reached, a conductive network is formed as conductive nanomaterials create tunneling electric paths within the insulative matrix, enabling efficient electron transport [123]. The presence of a well-connected conductive network ensures a consistent electrical conductivity, contributing to the long-term stability and reproducibility for the sensor's measurements. Conversely, in insulative materials or conductive nanocomposites below the percolation threshold, the dominant mechanism is hopping, resulting in frequency dependent behavior of AC conductivity, reduced sensitivity, and instability [124]. The impact of cyclohexane concentration on AC conductivity can be inferred from this graph. Increment in the void fraction widens the distance between graphene sheets, resulting in a decrease in electrical conductivity [125]. This trend is exemplified by considering the AC conductivity at 0.1 Hz in G-PDMS43, which exhibits AC conductivity of 0.25×10^{-3} S.cm^{-1} with 82.6% void fraction, compared to G-PDMS87 with a void fraction of 64.8% and AC conductivity of 3.5×10^{-3} S.cm^{-1}. The variation in conductivity is attributed to changes in the connectivity of the conductive network during the foaming process of the composite. Since the growth of air bubbles leads to re-orientation and displacement of the conductive network. Increasing the number of soft ice crystal templates pushes apart the pre-existing interconnected paths, reducing the likelihood of forming a conductive network [126]. Therefore, the electrical conductivity of the fabricated sensors can be modulated by controlling the void fraction through solvent concentration.

It is important to note that the behavior of AC conductivity can be characterized by two distinct regions with respect to the applied frequency. At lower frequencies, it is considered as Direct Current (DC) conductivity, which is frequency independent, and results in negligible polarization of electrodes. However, as the frequency suppresses the characteristic frequency (ωc), the conductivity exhibits a frequency-dependent behavior and increases with frequency. This frequency dependence of AC conductivity can be mathematically represented by the universal dynamic response (UDR) equation proposed by Jonscher [127] as follows: $\sigma_{AC} = \sigma_{DC} + A\omega^{s}$

where σ_{AC} and σ_{DC} is AC conductivity and DC conductivity, respectively. A is a temperature-dependent constant and ω is the angular frequency. The exponent value *S*, ranging from 0 to 1, is a frequency-dependent parameter depends on the temperature and pressure which governs the conduction mechanism in variety of materials [128,129]. Therefore, measuring the AC conductivity of a material at a low frequency, such as 0.1 Hz, can provide information about its DC conductivity [124]. However, in this study, the DC conductivity was assessed using the LSV method, which involves a through-plane

four-point probe analyzer. The following equations were used to calculate the DC conductivity: $R = {}^{V}/_{I}$ and $\sigma_{DC} = {}^{1}/_{\rho} = {}^{t}/_{A.R}$

where R is the electrical resistance that is calculated by the voltage (V) and current (I) applied to the sensors. The DC conductivity (σ_{DC}) can be obtained by taking the reciprocal of the electrical resistivity (ρ) of a material. The resistivity can be also computed by using the relationship between the thickness (t) and cross-sectional area (A) of the sensor, as well as its resistance [130]. As shown in Figure 4.6b, the trend of DC conductivity is similar to that of AC conductivity as expected with nearly the same values. For instance, the DC conductivity of PDMS43 is 0.13×10^{-3} S.cm^{-1}, while G-PDMS87 exhibits a DC conductivity of 3.11×10^{-3} S.cm^{-1}.

Electrical analysis was further performed to understand the impact of dielectric characteristics on the sensor's performance. The ability of materials to store electrical energy through the displacement of bound charges from their equilibrium positions under an applied electric field is known as polarization. This is represented by complex permittivity, defined as : $\varepsilon(\omega) = \varepsilon'(\omega) - i\varepsilon''(\omega)$ [131], where ω is angular frequency, $\varepsilon'(\omega)$ and $\varepsilon''(\omega)$ are the real permittivity and imaginary permittivity, respectively.

Figure 4.6c illustrates the measurement of the broadband real permittivity (ε') of G-PDMS microcellular structures over a frequency range of 10^{+1} to 10^{6} Hz, aiming to understand the underlying mechanisms. The observed trends in the real permittivity spectra across the measured frequency range can generally be attributed to various mechanisms, including interfacial, dipolar and nanofiller polarization. In heterogenous materials like composites, the mismatch of conductivity and permittivity values between the polymer matrix and nanomaterials leads to interfacial polarization, known as Maxwell-Wagner-Sillars effect [132]. Under applied electric field, charges migrate through the material, and their limited movement causes charge accumulation at the interface, resulting in interfacial polarization in the low frequency range of 10^{-6} to 1 Hz. At low frequencies, there is sufficient time for charges to migrate at the interfaces and form large dipoles. Therefore, as frequency increases, the interfacial polarization diminishes. Dipolar polarization, additionally, arises from the oriented dipoles of the asymmetric functional groups in the polymer matrix, where the Si atom exhibits different electrical dipolar moments compared to C and H atoms in the PDMS monomer. The strength of induced electric dipole moments formed during the polarization process is directly proportional to the applied electric field's intensity. In addition, nanofiller polarization refers to the polarization occurring in nanomaterials as a result of their localized topological defects. This phenomenon can generate magnetic

moments and spin polarization in carbonaceous nanomaterials when subjected to an applied electric field, even in the absence of a magnetic field or magnetic impurities [133,134].

Overall, multiple polarization mechanisms are at play in this system. In the low-frequency range, interfacial polarization becomes significant but gradually decreases with increasing frequency. Additionally, dipolar polarization arises due to the dipolar mismatch of functional groups of the polymer matrix and the nanofiller mismatch caused by the topological defects of graphene flakes produced by Hummer's method. As illustrated in Figure 4.6c, G-PDMS87 exhibits the highest value of real permittivity, whereas G-PDMS43 demonstrates the lowest value among the tested samples. This suggests that as porosity increases, the real permittivity decreases due to reduced charge accumulation at the polymer/graphene cell interfaces and fewer interfacial areas which are filled with air pockets.

Figure 4.6d illustrates the dielectric loss (tanδ) values for porous G-PDMS nanocomposites, providing insights into the dissipation of electrical energy. Typically, the frequency-dependent behavior of tanδ spectra is attributed to the conductivity loss at low frequencies and relaxation polarization losses at high frequencies [135]. Conductivity loss, primarily occurring at filler-filler junctions within composites, diminishes as frequency increases. At low frequencies, electrons have ample time to traverse through the conductive network, while at higher frequencies, their movement is limited to a few nanofiller clusters [136]. As presented in Figure 4.6d, a significant decrease in tanδ spectra of G-PDMS microcellular structures across the measured frequency range is observed. The values at low frequencies indicate conductivity loss, commonly known as ohmic loss, which surpasses relaxation polarization loss at high frequencies. This behavior is particularly dominant for nanocomposites at or above the percolation threshold [137,138]. G-PDMS87 exhibits the highest levels of ohmic loss, possibly due to its elevated conductivity values, leading to substantial current leakage. Conversely, G-PDMS43 exhibits the lowest dielectric loss values, may be attributed to the presence of fewer conductive filler-filler junctions for electron transportation.

Figure 4.6e presents the measured ε' and tanδ values at a representative frequency of 10^3 Hz to compare the dielectric properties of G-PDMS porous monoliths. It is evident that G-PDMS87 demonstrates superior ε' at 3800, which is 9.5 times higher than that of G-PDMS43. This observation can be attributed to the increased interfacial polarization occurring in foams with lower void fraction. This is a result of a higher number density of the polymer-nanomaterial clusters in a specific area, making parallel plate nanocapacitors. The tanδ values also follow a similar trend to ε', indicating that the

induced polarization within the conductive network leads to current leakage and dissipation of electrical energy. Consequently, G-PDMS87 exhibits a tanδ value of 3100, which is 385% higher than that of G-PDMS43, owing to the larger number of graphene-graphene junctions present in the low void fraction structure.

The sensitivity of G-PDMS foams with different morphological structures was assessed by evaluating their electromechanical performance. Figure 4.6f presents the resistance response of the sensors subjected to a compressive strain of up to 85% at a rate of 1 $mm.min^{-1}$, while the slope of the curve representing the gauge factor (GF) calculated using the formula provided in the experimental section. The collected data indicated a consistent trend among all G-PDMS microcellular nanocomposites, wherein an increase in strain corresponded to an increased resistance variation ($\Delta R/R_0$). The resistance response of the sensors could be divided into two main regions: (i) 0% to 10% strain, and (ii) strains of 10% and above.

In the first region, applying compression force led to a sharp rise in the resistance response, primarily due to the formation of a conductive path. The sharp increment was a result of intensified electron flow through the compressed conductive network, attributed to few point-to-point contacts of conductive network. Consequently, a significant decrease in resistance value was observed compared to the uncompressed state. In the second region, the resistance response gradually increased as further compression resulted in an increased contact area within the conductive network, thereby facilitating enhanced point-point connections and gradual increment in conductivity.

As a result, all microcellular structures in the first linear region exhibited higher sensitivity due to the abrupt change in resistance response. Specifically, G-PDMS43 displayed a GF of 0.08 in the first region, almost three times higher than the GF of G-PDMS87, which measured 0.028. These findings suggest that the change in resistance in higher porous structures is greater, attributed to the greater conductivity variance due to formation of a few point-to-point contacts. Conversely, in the second linear region, G-PDMS87 exhibited the highest GF value of 0.006 among all samples, while G-PDMS43 had the lowest GF of 0.0028, approximately half that of G-PDMS87. This outcome indicates that the resistivity variance in higher void fraction structures may not be as distinguishable. This can be attributed to the higher initial resistance value or less contact area connection while compression. In other words, resistance response did not change significantly upon compression because the conductive network failed to achieve complete connection between cells enabling transportation of electrons. As

an overview, cellular networks with lower porosity and a higher volume fraction of conductive nanomaterials demonstrate smaller resistance when compressed.

However, it is crucial to consider all the properties of fabricated sensors to meet the requirements of wearable and flexible application, including electrical and mechanical properties. Therefore, sensitivity alone is not sufficient; mechanical characteristics also play a significant role. For instance, G-PDMS43 foam with a void fraction of 64%, can be compressed up to 70%, while G-PDMS87 is compressible up to 85% with void fraction of 82%. Among the fabricated sensors, G-PDMS70 exhibits a high compressibility of up to 80%, exceeding that of G-PDMS43 and G-PDMS48, which have compressibility levels of 70% and 75%, respectively. Moreover, G-PDMS70 has higher gauge factor values compared to G-PDMS77 and G-PDMS87 in the second linear range of resistance response curves, owing to its lower porosity providing lower values of out-of-plane resistance as well as a lower initial resistance value due to higher graphene concentration in unit volume. Therefore, when fabricating sensors, the resistance response curve should be considered across the entire detection window for more reliable and broader applications. Consequently, a linear response and higher gauge factor over the detection range are favorable.

It is important to note that the mechanical properties offer insights into the compressive strength, modulus, and compressive strain of the fabricated porous foams. Since the cell-wall thickness and porosity impact the mechanical characteristics of porous nanocomposites, mechanical testing was conducted to measure the compressive strength, modulus, and compressibility of cellular nanocomposites. This helps in better understanding the impact of the morphological structure on mechanical performance.

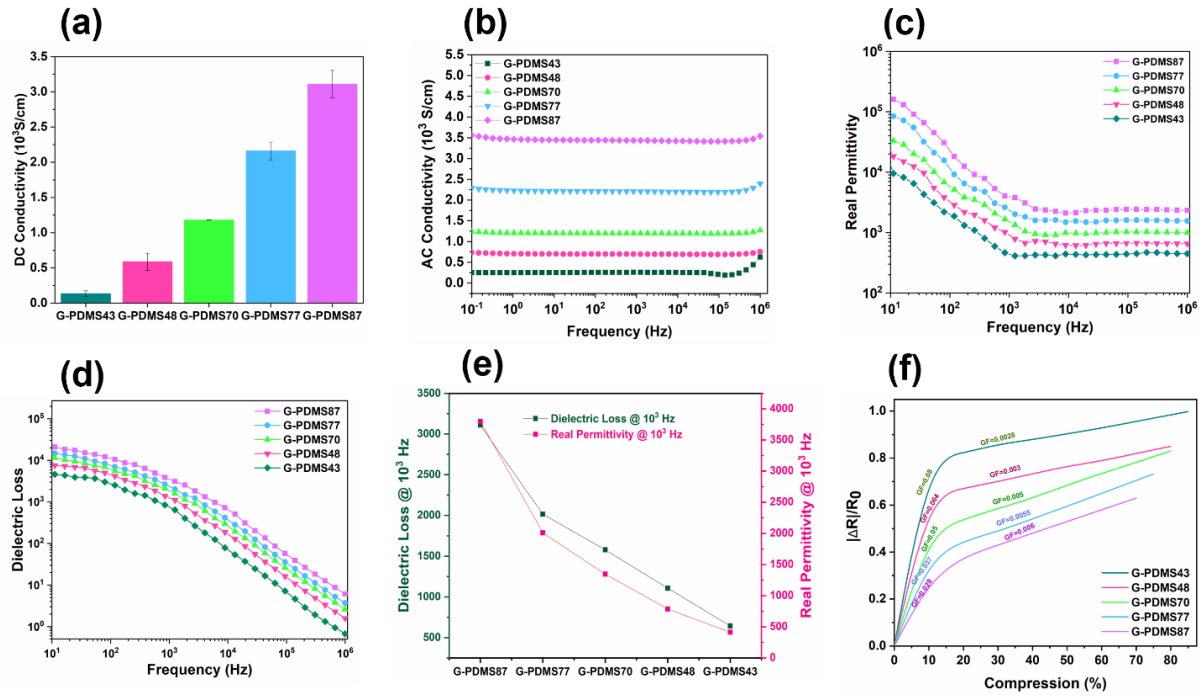


Figure 4.6 (a) DC electrical conductivity, (b) broadband AC electrical conductivity, (c) real permittivity, (d) dielectric loss, (e) comparison of dielectric properties at the frequency of 10^3 Hz for G-PDMS foams, and (f) resistance change curves of G-PDMS foams under compressive strains.

4.4.4 Mechanical properties of G-PDMS sensors

To investigate the effect of the morphological structure of sensors on mechanical properties, typical stress-strain curves of G-PDMS foams were measured. All porous samples were subjected to loading/unloading compression testing, ranging from 10% to 85% compressive strain, under constant rate of 1 $mm.min^{-1}$, as depicted in Figure 4.7. While the shape of the stress-strain curve remained consistent for all samples, there were variations in mechanical properties such as compressive strength, maximum compressive strain, and elastic modulus, as summarized in Table 4.4. The mechanical behavior of samples, shown in stress-strain curves, could be categorized in three regions. At compressive strains below 10%, the linear elastic regions were observed due to the elastic bending of cell structures [139]. The measured Young's modulus of the specimens ranged from 27.13 to 219.64 kPa, indicating that an increase in the void fraction from 65 to 82% resulted in a substantial 98% decrease in the Young's modulus. Within the compressive strain range of 20 to 60%, densification of

cell structures became evident, followed by a sharp increase in compressive strength from 60 to 85%. For instance, G-PDMS43 exhibited an increase of 45.8 kPa in compressive strength from 20 to 60% strain. While from 60 to 85% strain, the compressive strength showed an abrupt increase of 770 kPa, which is about 17 times higher than that of 20 to 60% strain. At high compressive strains of 80% and 85%, the cell walls experienced substantial compression force, resulting in the complete contact of pore sites, preventing further compression [140].

The high compressibility and excellent compressive strength of the synthesized foams can be attributed to the disordered macroporous design of the structure, which could be adjusted by varying the volume concentration of the cyclohexane in the mixture. As shown in Table 4.4 and Figure 4.7, the mechanical properties of the sensors depend on the morphological structure, specifically porosity and weight density. Decreasing the weight density through increased porosity results in network's structure with lower void fraction and smaller pore sizes. This kind of structures exhibit resistance to lower strain yields while offering higher compressive strength due to the presence of thicker connected cell-walls in the network. For instance, G-PDMS87 (Figure 4.7a) demonstrated a compressibility of 70%, with a compressive strength of 1500 kPa at 70% compressive strain. While G-PDMS43 (Figure 4.7b) with a high void fraction of 82%, can be compressed up to 85% with a compressive strength of 115 kPa at 70% compressive strain, approximately 10 times lower than that of G-PDMS87. Additionally, G-PDMS70 (Figure 4.7c) exhibited a mechanical strength of 447 kPa at 70% compressive strain and compressibility of 80%, with an elastic modulus of 61 kPa. The broad range of mechanical behavior observed in the fabricated foams highlights the tunability of this fabrication method and underscores the potential application of them in a wide range of high-pressure sensing detection devices.

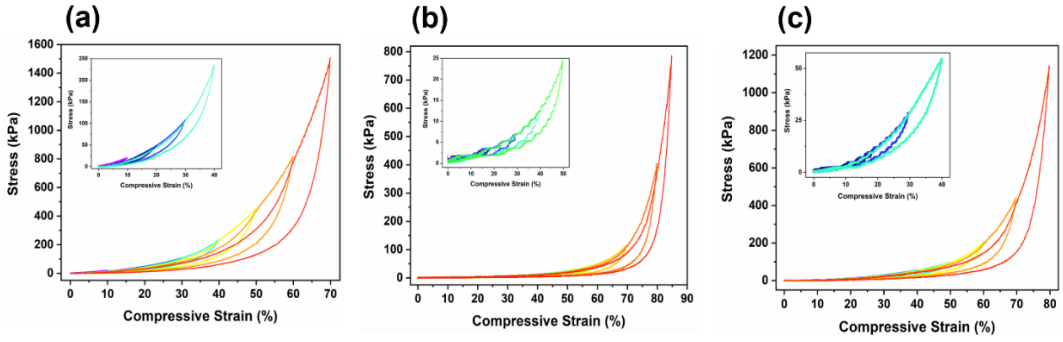


Figure 4.7 Compressive stress-strain curve of (a) G-PDMS87, (b) G-PDMS43, and (c) G-PDMS70.

Table 4.4 Extracted parameters from mechanical testing.

	Mechanical properties			
Sample	**Elastic Modulus (kPa)**	**Compressive Strength at 70% Compression (kPa)**	**Maximum Compressive Strain (%)**	**Compressive Strength at Maximum Compression (kPa)**
G-PDMS43	27.13	115.27	85	787.72
G-PDMS48	37.31	189.62	80	547.65
G-PDMS70	61.07	447.24	80	1147.36
G-PDMS77	120.67	1392.7	75	2034.21
G-PDMS87	219.64	1508.60	70	1508.60

4.4.5 Fatigue resistance and piezoresistivity testing of G-PDMS70

The mechanical robustness of 3D porous foams for pressure sensing applications can be evaluated through analysis of cyclic fatigue resistance testing as shown in Figure 4.8a and Figure 4.8b. Figure 4.8a illustrates the compressive loading/unloading behavior of G-PDMS 70 at various cycle numbers (10th, 50th, 100th, 250th, and 500th cycles). It can be observed that all cyclic mechanical tests exhibited consistent behavior, indicating the mechanical robustness of the foam structures without any noticeable changes in the cell structures. Furthermore, stress retention, which characterizes the maximum compressive stress reached after each cyclic test, was analyzed. It was found that G-PDMS70 exhibited a reduction of approximately 10% in stress retention after applying 500 compressive loading/unloading testing. Figure 4.8b shows the compressive stress deviations during the time of loading/unloading cycles. It suggests the robust behavior of sensor during the cycles. Overall, the mechanical durability and resilience of the fabricated 3D porous foam structures supports their suitability for pressure sensing applications. Energy loss coefficient (shown in Figure 4.8c) was calculated by equation described in the experimental section. Work of loading and work of unloading process were calculated by the area of the compression and release process in each cycle in the MATLAB software. The work used for the first cycle is higher than the other cycles, indicating the irreversible damage caused by stress to the cellular structures. Therefore, in the first cycle more energy was consumed for pressing the porous structure to dense the cellular structure to lower thickness than the other cycles. Energy absorption is a

property of the cellular structures[140] that dissipate the energy within their network and could be represented as a parameter of energy loss coefficient. The energy loss coefficient for G-PDMS70 was initially calculated to be 0.22 and remained almost constant from the 10th cycle to the 500th cycle, recommending the stability of the cellular structure under continues cyclic loading/unloading compression process. Stress retention describes the maximum compressive stress that a material reaches after each cyclic testing. It was analyzed for the 10, 50, 100, 250, and 500th cycle of both sensors and plotted in Figure 4.8c. The maximum compressive energy after 500 cycles decreased about 10% from its initial value for the foam consisted of only 0.68 Vol.% graphene.

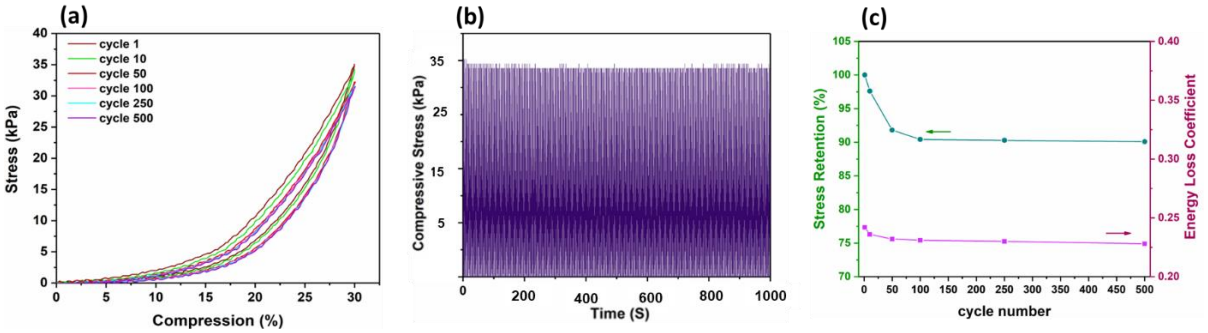


Figure 4.8 Cyclic compressive stress-strain curves for G-PDMS70 with the rate of 3 mm.min-1 under maximum compressive strain of 30%, (b) Cyclic compressive testing at the maximum compressive strain of 30% for G-PDMS70, (c) extracted parameters of cyclic testing for G-PDMS70.

To investigate the stimulus response (static and dynamic behavior) of the fabricated foams, G-PDMS70 was subjected to testing using a universal testing machine and tapping testing. As shown in Figure 4.9a, constant pressure of 29 kPa was applied to achieve a 30% compressive strain at different speed rates to G-PDMS70. It can be observed that increasing the rate of applied pressure results in faster response, confirming their genuine sensing properties. The reproducible peaks over 5 cycles demonstrate the ability of the fabricated sensors to produce well-defined responses that can be interpreted using suitable algorithms. Moreover, flexible G-PDMS70 sensor successfully achieved real-time monitoring of human motion. As depicted in Figure 4.9b, it was capable of distinguishing different states of compression induced by finger tapping, such as the intensity and duration of the compressive strain, by analyzing periodic changes in resistance. Variations in the curve shape and current intensity obtained by the sensor indicated the number and interval of each finger tap. During the application of pressure,

the current passing through the sensor increased from 0.1 mA to 0.2 mA and then returned to 0.1 mA within 1 ms upon relaxation. This demonstrates the excellent recovery time and shape memory performance of the 3D foam sensors and the ability to instantly and accurately detect pressure changes with reproducible data. Moreover, they exhibit stability and ease of processing with the new one-pot synthesis method, showcasing their potential for application in wearable electronic devices.

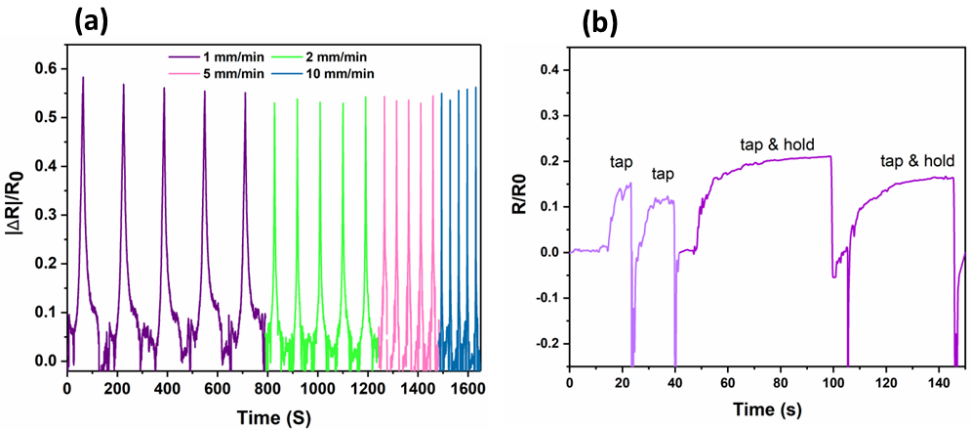


Figure 4.9 (a) 5 cyclic compression-electric sensing curve of G-PDMS70 with different compression rate at fixed 30% compressive strain, (b) actual piezoresistive sensing performance by tap testing.

4.5 Conclusion

In this project, we introduced a novel one-pot soft-templating method for fabricating PDMS-based conductive compressive sensors. Highly porous 3D structure was obtained by evaporation of the soft templates of cyclohexane's ice crystals. Different pore size and void fractions were obtained by optimizing the solvent concentration. It was found that the addition of 0.43 vol% graphene, the microcellular nanocomposite showed electrical conductivity of 2.5×10^{-2} S/m with the mechanical strength of 780 kPa at 85% compression strain. The exceptional compressibility of the foam was attributed to the strong 3D interconnected structure with a high void fraction (82%). Increasing the graphene concentration to 0.87 vol%, the electrical conductivity reached the value of 35×10^{-2} S/m and compressive strength showed 1500 kPa at 70% strain with the void fraction of 64.8%. The electromechanical performances of the porous nanocomposites were also thoroughly investigated. The

microcellular structures showed two linear resistance responses along the compressive strain range. Particularly, 0.43 vol% loaded foam showed an abrupt change in resistivity until 10 % strain and resulted in a high gauge factor of 0.5 kPa^{-1}. From 10 to 85% strain, the foam exhibited the second linear detection region with the gauge factor of 1.2 MPa^{-1}. The compressive sensors also showed very fast response time of 20 ms and outstanding cyclic stability of 500 cycles due to their robust 3D interconnected structure, suggesting its suitability for mid and high-pressure sensing applications and real-time monitoring of human joint movements.

As an overview, the results obtained from this study are compared to the literature, presented in the Table 4.5. This table was specifically chosen based on microcellular graphene-based polymer nanocomposites. Overall, the findings presented in this research contribute significantly to the advancement of wearable electronic devices, emphasizing the potential of the developed compressive sensors for diverse applications in real-time health monitoring and robotics. The simplicity and cost-effectiveness of the proposed fabrication method open up new avenues for the scalable production of wearable sensors with tailored properties, further propelling innovations in the electronic industry.

Table 4.5 Comparison of results with other microcellular graphene-based polymer nanocomposites in literature.

Matrix	Nano-particles	Fabrication Method	Sensitivity*	Response time	Stability (cycles)	Compressive strain range (%)	Process	Ref.
PDMS	Graphene	Chemical foaming	Region1: 5.89 Region2: 32.9	200 ms	1000 (at 10% strain)	Region1: 0-20 Region2: 20-40	One-pot synthesis	[141]
PU	Graphene	Freeze casting	Region1: 2.45 Region2: 12.24	NA	50	Region1: 0-60 Region2: above 60	One-pot synthesis	[142]
PU foam	rGO	Dip-coating	0.067 kpa^{-1}	10 ms (at 150 Pa)	10000 (at 150 Pa)	NA	Multiple step synthesis	[143]

PI foam	graphene	Dip-coating	Region1:0.36 kPa^{-1} Region2: 0.01 kPa^{-1}	80 ms (2 Kpa)	1000 (at 15%)	0-50	Multiple step synthesis	[144]
PDMS	graphene	Dip-coating	Region1: 2.87 Region2: 2.87-8.77	NA	36,000 (at 5% strain)	Region1: 0-10 Region2: 10-50	Multiple step synthesis	[145]
PU	graphene	Dip-coating and Freeze casting	0.75 kPa^{-1} to 3.08 kPa^{-1}	14 ms	10000	0−99	Multiple step synthesis	[146]
PI	rGO	Freeze casting and Thermal annealing	Region1 (0-1.5 kPa):0.18 kPa^{-1} Region2 (3.5-6.5 kPa): 0.023 kPa^{-1}	NA	2000	0-50	Multiple step synthesis	[147]
PDMS	graphene	Soft Templating	Region1: 0.5 kPa^{-1} Region2: 1.2 MPa^{-1}	20 ms	500 (at 30% strain)	0-85	One-pot synthesis	This Study

*The dimensionless sensitivity values were calculated by the $S=(\Delta R/R_0)/\varepsilon$ for reference 141, 142, and 145, whereas sensitivity values for reference 143, 144, 146, and 147 were calculated by $S=(\Delta R/R_0)/P$

Chapter 5
Conclusion and Recommendations

5.1 Conclusions

Polymers have become crucial components in developing advanced functional materials due to their lightweight-ness, mechanical robustness, chemical resistance, and easy processibility. These materials are used in compact electronic devices, physical sensors, EMI shielding materials, and energy storage devices by fabricating versatile combinations of polymer matrices with different conductive nanomaterials. Various methods have been developed for the fabrication of electrically conductive nanocomposites, each with their unique benefits and drawbacks from an industrial perspective. Recently, compressive piezoresistive sensors have been developed based on diverse E-CPnCs, as metallic and semiconductor materials struggle to endure significant strains and maintain mechanical stability during prolonged use. Consequently, there is a growing need to address the fabrication of advanced materials for mechanical sensing applications. While different approaches have been explored in the literature for fabricating these devices, many of them involve complex and multi-step processes, lacking simplicity and cost-effectiveness from an industrial standpoint. Therefore, the primary objective of my research was to design and develop novel methods for fabricating electrically conductive microcellular polymer composites, specifically tailored for use as compressive piezoresistive sensors.

In this project, we employed a novel one-pot synthesis method to create a porous microcellular structure in solvent-based polymer nanocomposite systems. In this solvent-based system, a suitable solvent is required that can facilitate the formation of a pore structure while also functioning as a good solvent for the polymer and a dispersant for nanofillers. To fulfill these requirements, graphene was used as conductive nanofillers within a PDMS elastomeric matrix. Cyclohexane, an engineered solvent, was employed in this system to generate pores within the structure through evaporation under specific temperature and pressure conditions.

Using this method, a mixture of nanofiller, solvent, and solvent-based elastomer was prepared. By controlling the temperature and pressure, a porous structure was formed through the evaporation of the solvent, acting as a soft template. Graphene, as a conductive nanomaterial, was dispersed in varying

amounts of cyclohexane, and PDMS and its curing agent were added to the mixture. The resulting mixture was freeze-dried, and the evaporation of cyclohexane crystals within the structure by considering solvent's triple point results in the formation of pores. Consequently, porous structures with different levels of porosity were fabricated. The electrical properties of fabricated foams were assessed using impedance spectroscopy. By coupling the electrochemical workstation with the universal testing machine (UTM), the electromechanical properties of the fabricated compressive piezoresistive sensor can be studied. Moreover, the mechanical properties and robustness of compressive sensors were evaluated through compression testing of UTM. Finally, a discussion was conducted on how the porosity of the structure affects the electrical performance, mechanical properties, and sensitivity of the piezoresistive sensors.

5.2 Recommendations

Despite significant advancement in this field, there are still areas that require further development and exploration of microcellular conductive polymer nanocomposites. The exploration could be engineering physical tactile sensors with higher sensitivity, mechanical robustness and workability. For example, one such area highlights enhancing mechanical performance of flexible wearable sensors, involving fabrication of devices for real-time monitoring of human health conditions, posture recognition and exercise performance analysis wherein the sensors should be easily attachable to the body while retaining their robustness and stability. Additionally, the excellent mechanical properties of piezoresistive sensors used in the industrial automation devices ensure their long-term workability. Another research area focuses on the fabrication of ultra-sensitive piezoresistive sensors. For example, the creation of highly sensitive sensors designed to measure the aging of batteries involves integrating a sensor with a Li-ion battery. The sensor detects minute changes in the thickness of the battery, attributed to the expansion effect. It's crucial to highlight that the detection accuracy should be on the micrometer scale. Furthermore, ultra-sensitive pressure sensors could play a pivotal role in detecting heartbeat patterns and respiratory rates, aiding in monitoring the health conditions of individuals requiring assistance. Achieving higher sensitivity necessitates the modification of the electrical response of fabricated sensors. Another area of research focuses on enhancing the functionality and workability of these devices, which are prone to electromagnetic waves in their surrounding environment. Regarding the inevitable impact of EMI pollution on the sensor's functionality, it is

crucial to develop multifunctional nanocomposites with the ability to integrate both mechanical sensing and EMI protection within a single device. It should be noted that these advanced capabilities can be engineered through a combination of material control and process control methodologies in fabricating E-CPnCs.

5.2.1 Material research

- Investigate the influence of different carbonaceous nanomaterials with different structures on electrical, mechanical and electromechanical performance of compressive piezoresistive sensors. The electromagnetic shielding efficiency of them can be studied as well to design multifunctional advanced electronic devices.

5.2.2 Processing research

- Different processing techniques can be explored for developing E-CPnCs. Freeze casting, for instance, is a tunable environmentally friendly method for fabricating cellular composites. Unidirectional freeze drying induces the alignment of nanomaterials along the direction of ice crystal growth. Initial findings indicate a variance in the electrical conductivity of the nanocomposites in the alignment direction compared to the normal direction. Given that EMI shielding, and sensitivity is influenced by electrical conductivity, investigating the impact of nanomaterial alignment on the electromechanical and EMI shielding performance of the nanocomposite is a worthwhile avenue for research. Foaming method is also a versatile method for fabrication of cellular E-CPnCs. By this method, different porous structures are fabricated varied by different density. Since the pore size distribution has impact on the mechanical properties of cellular composites, and the impedance mismatch within the cellular E-CPnCs, it is worthy to study on this parameter in the future studies.
- Tunning cellular composites can be further engineered by the gradient and sandwich like structures. Since heterogenous cellular structures have impact on the sensitivity range and the impedance mismatch of the materials within the composite.

For instance, the following studies will focus on various parameters involved in the fabrication of conductive nanocomposites with different fabrication methods across multifunctional applications, including:

I. Assessing the impact of nanomaterial orientation on electromechanical and EMI SE properties of microcellular networks

This project focuses on the development of a novel dual-function device that combines piezoresistive sensing with EMI shielding capabilities. This device has significant potential in applications where simultaneous monitoring of mechanical forces and protection against electromagnetic waves are critical. The controlled microstructure of the cellular structure plays a crucial role in developing this multifunctional device. Therefore, freeze-casting will be employed to fabricate microcellular structures with controlling nanomaterials alignment within the matrix. Both unidirectional and bi-directional freeze-casting methods could be utilized to study the effects of alignment and orientation of nanomaterials on the electrical and mechanical performance of the nanocomposite, resulting in differently ordered microcellular structures. The resulting structure plays a decisive role in the conductive network formation and the mechanical properties of anisotropic nanocomposites.

II. Investigating impact of gradient porosity and conductivity on microcellular nanocomposites properties

The aim of this project is to enhance the sensitivity, detection range and the shielding effectiveness of dual piezoresistive sensors and EMI shielding devices. Thus, a hierarchical microstructure could be designed to satisfy this target. As expected, gradient porous structures can be used as compressive piezoresistive sensors with larger detection limit and also the capability of absorbing EM waves through higher interfacial areas for absorption.

References

[1] R. Yin, D. Wang, S. Zhao, Z. Lou, G. Shen, Wearable sensors-enabled human–machine interaction systems: from design to application, Adv Funct Mater 31 (2021) 2008936.

[2] Y. Liu, K. He, G. Chen, W.R. Leow, X. Chen, Nature-inspired structural materials for flexible electronic devices, Chem Rev 117 (2017) 12893–12941.

[3] M. Panahi-Sarmad, M. Noroozi, M. Abrisham, S. Eghbalinia, F. Teimoury, A.R. Bahramian, P. Dehghan, M. Sadri, V. Goodarzi, A Comprehensive Review on Carbon-Based Polymer Nanocomposite Foams as Electromagnetic Interference Shields and Piezoresistive Sensors, ACS Appl Electron Mater 2 (2020) 2318–2350. https://doi.org/10.1021/acsaelm.0c00490.

[4] Y. Cao, Y. Meng, Y. Jiang, S. Qian, D. Fan, X. Zhou, Y. Qian, S. Lin, T. Qian, Q. Pan, Healable supramolecular phase change polymers for thermal energy harvesting and storage, Chemical Engineering Journal 433 (2022) 134549. https://doi.org/https://doi.org/10.1016/j.cej.2022.134549.

[5] X. Li, Y. Wang, Y. Zhao, J. Zhang, L. Qu, Graphene Materials for Miniaturized Energy Harvest and Storage Devices, Small Struct 3 (2022) 2100124. https://doi.org/https://doi.org/10.1002/sstr.202100124.

[6] K. Tian, D. Hu, Q. Wei, Q. Fu, H. Deng, Recent progress on multifunctional electromagnetic interference shielding polymer composites, J Mater Sci Technol 134 (2023) 106–131. https://doi.org/https://doi.org/10.1016/j.jmst.2022.06.031.

[7] E. Sazonov, Wearable Sensors: Fundamentals, Implementation and Applications, Elsevier Science, 2020. https://books.google.ca/books?id=F9PVDwAAQBAJ.

[8] A. Barhoum, Z. Altintas, Advanced Sensor Technology: Biomedical, Environmental, and Construction Applications, Elsevier Science, 2022. https://books.google.ca/books?id=vzJcEAAAQBAJ.

[9] R. Banerjee, A. Gebrekrstos, J.T. Orasugh, S.S. Ray, Nanocarbon-Containing Polymer Composite Foams: A Review of Systems for Applications in Electromagnetic Interference Shielding, Energy Storage, and Piezoresistive Sensors, Ind Eng Chem Res 62 (2023) 6807–6842. https://doi.org/10.1021/acs.iecr.3c00089.

[10] S. Yang, P. Yang, C. Ren, X. Zhao, J. Zhang, Millefeuille-inspired highly conducting polymer nanocomposites based on controllable layer-by-layer assembly strategy for durable and stable electromagnetic interference shielding, J Colloid Interface Sci 622 (2022) 97–108. https://doi.org/https://doi.org/10.1016/j.jcis.2022.04.096.

[11] K.-Y. Chen, Y.-T. Xu, Y. Zhao, J.-K. Li, X.-P. Wang, L.-T. Qu, Recent progress in graphene-based wearable piezoresistive sensors: From 1D to 3D device geometries, Nano Materials Science (2022). https://doi.org/https://doi.org/10.1016/j.nanoms.2021.11.003.

[12] S. Jung, J.H. Kim, J. Kim, S. Choi, J. Lee, I. Park, T. Hyeon, D. Kim, Reverse-micelle-induced porous pressure-sensitive rubber for wearable human–machine interfaces, Advanced Materials 26 (2014) 4825–4830.

[13] Y. Wu, I. Karakurt, L. Beker, Y. Kubota, R. Xu, K.Y. Ho, S. Zhao, J. Zhong, M. Zhang, X. Wang, Piezoresistive stretchable strain sensors with human machine interface demonstrations, Sens Actuators A Phys 279 (2018) 46–52.

[14] W. Cao, Y. Luo, Y. Dai, X. Wang, K. Wu, H. Lin, K. Rui, J. Zhu, Piezoresistive Pressure Sensor Based on a Conductive 3D Sponge Network for Motion Sensing and Human–Machine Interface, ACS Appl Mater Interfaces (2023).

[15] T. Yang, X. Jiang, Y. Huang, Q. Tian, L. Zhang, Z. Dai, H. Zhu, Mechanical sensors based on two-dimensional materials: Sensing mechanisms, structural designs and wearable applications, iScience 25 (2022) 103728. https://doi.org/https://doi.org/10.1016/j.isci.2021.103728.

[16] G. Canavese, S. Stassi, C. Fallauto, S. Corbellini, V. Cauda, V. Camarchia, M. Pirola, C.F. Pirri, Piezoresistive flexible composite for robotic tactile applications, Sens Actuators A Phys 208 (2014) 1–9.

[17] M. Xie, K. Hisano, M. Zhu, T. Toyoshi, M. Pan, S. Okada, O. Tsutsumi, S. Kawamura, C. Bowen, Flexible multifunctional sensors for wearable and robotic applications, Adv Mater Technol 4 (2019) 1800626.

[18] Z. Shi, L. Meng, X. Shi, H. Li, J. Zhang, Q. Sun, X. Liu, J. Chen, S. Liu, Morphological engineering of sensing materials for flexible pressure sensors and artificial intelligence applications, Nanomicro Lett 14 (2022) 141.

[19] Q. Sun, Q. Lai, Z. Tang, X. Tang, X. Zhao, V.A.L. Roy, Advanced Functional Composite Materials toward E-Skin for Health Monitoring and Artificial Intelligence, Adv Mater Technol (2022) 2201088.

[20] X. Yang, M. Zhang, S. Gong, M. Sun, M. Xie, P. Niu, W. Pang, Chest-Laminated and Sweat-Permeable E-Skin for Speech and Motion Artifact-Insensitive Cough Detection, Adv Mater Technol (2022) 2201043.

[21] Y. He, L. Zhao, J. Zhang, L. Liu, H. Liu, L. Liu, A breathable, sensitive and wearable piezoresistive sensor based on hierarchical micro-porous PU@ CNT films for long-term health monitoring, Compos Sci Technol 200 (2020) 108419.

[22] L. Ma, T. Xia, R. Yu, X. Lei, J. Yuan, X. Li, G.J. Cheng, F. Liu, A 3D-Printed, Sensitive, Stable, and Flexible Piezoresistive Sensor for Health Monitoring, Adv Eng Mater 23 (2021) 2100379.

[23] M.S. Irfan, T. Khan, T. Hussain, K. Liao, R. Umer, Carbon coated piezoresistive fiber sensors: From process monitoring to structural health monitoring of composites–A review, Compos Part A Appl Sci Manuf 141 (2021) 106236.

[24] Y. Song, H. Chen, Z. Su, X. Chen, L. Miao, J. Zhang, X. Cheng, H. Zhang, Highly compressible integrated supercapacitor–piezoresistance-sensor system with CNT–PDMS sponge for health monitoring, Small 13 (2017) 1702091.

[25] K. Ke, V. Solouki Bonab, D. Yuan, I. Manas-Zloczower, Piezoresistive thermoplastic polyurethane nanocomposites with carbon nanostructures, Carbon N Y 139 (2018) 52–58. https://doi.org/https://doi.org/10.1016/j.carbon.2018.06.037.

[26] H. Ma, X. Zhang, L. Yang, L. Ma, C.B. Park, P. Gong, G. Li, Electromagnetic wave absorption in graphene nanoribbon nanocomposite foam by multiscale electron dissipation of atomic defects, interfacial polarization and impedance match, Carbon N Y 205 (2023) 159–170. https://doi.org/https://doi.org/10.1016/j.carbon.2023.01.028.

[27] X. Tang, P. Pötschke, J. Pionteck, Y. Li, P. Formanek, B. Voit, Tuning the Piezoresistive Behavior of Poly(Vinylidene Fluoride)/Carbon Nanotube Composites Using Poly(Methyl Methacrylate), ACS Appl Mater Interfaces 12 (2020) 43125–43137. https://doi.org/10.1021/acsami.0c11610.

[28] L. Wang, Z. Ma, Y. Zhang, L. Chen, D. Cao, J. Gu, Polymer-based EMI shielding composites with 3D conductive networks: A mini-review, SusMat 1 (2021) 413–431. https://doi.org/https://doi.org/10.1002/sus2.21.

[29] Z. Sang, K. Ke, I. Manas-Zloczower, Design Strategy for Porous Composites Aimed at Pressure Sensor Application, Small 15 (2019) 1903487. https://doi.org/https://doi.org/10.1002/smll.201903487.

[30] K. Qian, J. Zhou, M. Miao, H. Wu, S. Thaiboonrod, J. Fang, X. Feng, Highly Ordered Thermoplastic Polyurethane/Aramid Nanofiber Conductive Foams Modulated by Kevlar Polyanion for Piezoresistive Sensing and Electromagnetic Interference Shielding, Nanomicro Lett 15 (2023) 88. https://doi.org/10.1007/s40820-023-01062-0.

[31] Z. Ma, X. Xiang, L. Shao, Y. Zhang, J. Gu, Multifunctional Wearable Silver Nanowire Decorated Leather Nanocomposites for Joule Heating, Electromagnetic Interference Shielding and Piezoresistive Sensing, Angewandte Chemie International Edition 61 (2022) e202200705. https://doi.org/https://doi.org/10.1002/anie.202200705.

[32] H. Guo, T. Hua, J. Qin, Q. Wu, R. Wang, B. Qian, L. Li, X. Shi, A New Strategy of 3D Printing Lightweight Lamellar Graphene Aerogels for Electromagnetic Interference Shielding and Piezoresistive Sensor Applications, Adv Mater Technol 7 (2022) 2101699. https://doi.org/https://doi.org/10.1002/admt.202101699.

[33] R. Taherian, A. Kausar, Electrical Conductivity in Polymer-Based Composites: Experiments, Modelling, and Applications, Elsevier Science, 2018. https://books.google.ca/books?id=1w5atAEACAAJ.

[34] P. Consortium, Introduction to Conductive Polymer Composites, Smithers Information Limited, 2011. https://books.google.ca/books?id=FAMmDwAAQBAJ.

[35] X. Huang, C. Zhi, Polymer Nanocomposites: Electrical and Thermal Properties, Springer International Publishing, 2016. https://books.google.ca/books?id=Du8gDAAAQBAJ.

[36] Prateek, V.K. Thakur, R.K. Gupta, Recent Progress on Ferroelectric Polymer-Based Nanocomposites for High Energy Density Capacitors: Synthesis, Dielectric Properties, and Future Aspects, Chem Rev 116 (2016) 4260–4317. https://doi.org/10.1021/acs.chemrev.5b00495.

[37] C.I. Idumah, Novel trends in conductive polymeric nanocomposites, and bionanocomposites, Synth Met 273 (2021) 116674. https://doi.org/https://doi.org/10.1016/j.synthmet.2020.116674.

[38] Y. Ling, T. An, L.W. Yap, B. Zhu, S. Gong, W. Cheng, Disruptive, Soft, Wearable Sensors, Advanced Materials 32 (2020) 1904664. https://doi.org/https://doi.org/10.1002/adma.201904664.

[39] H.C. Ates, P.Q. Nguyen, L. Gonzalez-Macia, E. Morales-Narváez, F. Güder, J.J. Collins, C. Dincer, End-to-end design of wearable sensors, Nat Rev Mater 7 (2022) 887–907.

[40] M.-Y. Liu, C.-Z. Hang, X.-F. Zhao, L.-Y. Zhu, R.-G. Ma, J.-C. Wang, H.-L. Lu, D.W. Zhang, Advance on flexible pressure sensors based on metal and carbonaceous nanomaterial, Nano Energy 87 (2021) 106181. https://doi.org/https://doi.org/10.1016/j.nanoen.2021.106181.

[41] K.-H. Ha, H. Huh, Z. Li, N. Lu, Soft capacitive pressure sensors: trends, challenges, and perspectives, ACS Nano 16 (2022) 3442–3448.

[42] S.R.A. Ruth, V.R. Feig, H. Tran, Z. Bao, Microengineering pressure sensor active layers for improved performance, Adv Funct Mater 30 (2020) 2003491.

[43] W. Chen, X. Yan, Progress in achieving high-performance piezoresistive and capacitive flexible pressure sensors: A review, J Mater Sci Technol 43 (2020) 175–188. https://doi.org/https://doi.org/10.1016/j.jmst.2019.11.010.

[44] X. Wei, X. Cao, Y. Wang, G. Zheng, K. Dai, C. Liu, C. Shen, Conductive herringbone structure carbon nanotube/thermoplastic polyurethane porous foam tuned by epoxy for high performance flexible piezoresistive sensor, Compos Sci Technol 149 (2017) 166–177.

[45] L. Yang, Y. Liu, C.D.M. Filipe, D. Ljubic, Y. Luo, H. Zhu, J. Yan, S. Zhu, Development of a highly sensitive, broad-range hierarchically structured reduced graphene oxide/polyhipe foam for pressure sensing, ACS Appl Mater Interfaces 11 (2019) 4318–4327.

[46] T. Zhai, L. Verdolotti, S. Kacilius, P. Cerruti, G. Gentile, H. Xia, M. Stanzione, G.G. Buonocore, M. Lavorgna, High piezo-resistive performances of anisotropic composites realized by embedding rGO-based chitosan aerogels into open cell polyurethane foams, Nanoscale 11 (2019) 8835–8844.

[47] T. Yang, D. Xie, Z. Li, H. Zhu, Recent advances in wearable tactile sensors: Materials, sensing mechanisms, and device performance, Materials Science and Engineering: R: Reports 115 (2017) 1–37.

[48] J.C. Yang, J. Mun, S.Y. Kwon, S. Park, Z. Bao, S. Park, Electronic skin: recent progress and future prospects for skin-attachable devices for health monitoring, robotics, and prosthetics, Advanced Materials 31 (2019) 1904765.

[49] Z. Liu, L. Htein, K.-K. Lee, K.-T. Lau, H.-Y. Tam, Large dynamic range pressure sensor based on two semicircle-holes microstructured fiber, Sci Rep 8 (2018) 65.

[50] L. Duan, D.R. D'hooge, L. Cardon, Recent progress on flexible and stretchable piezoresistive strain sensors: From design to application, Prog Mater Sci 114 (2020) 100617. https://doi.org/https://doi.org/10.1016/j.pmatsci.2019.100617.

[51] S. Li, J.G. Park, S. Wang, R. Liang, C. Zhang, B. Wang, Working mechanisms of strain sensors utilizing aligned carbon nanotube network and aerosol jet printed electrodes, Carbon N Y 73 (2014) 303–309.

[52] K. Ke, P. Pötschke, N. Wiegand, B. Krause, B. Voit, Tuning the Network Structure in Poly(vinylidene fluoride)/Carbon Nanotube Nanocomposites Using Carbon Black: Toward Improvements of Conductivity and Piezoresistive Sensitivity, ACS Appl Mater Interfaces 8 (2016) 14190–14199. https://doi.org/10.1021/acsami.6b03451.

[53] X. Li, T. Hua, B. Xu, Electromechanical properties of a yarn strain sensor with graphene-sheath/polyurethane-core, Carbon N Y 118 (2017) 686–698.

[54] T. Yang, X. Jiang, Y. Zhong, X. Zhao, S. Lin, J. Li, X. Li, J. Xu, Z. Li, H. Zhu, A Wearable and Highly Sensitive Graphene Strain Sensor for Precise Home-Based Pulse Wave Monitoring, ACS Sens 2 (2017) 967–974. https://doi.org/10.1021/acssensors.7b00230.

[55] A. Benchirouf, C. Müller, O. Kanoun, Electromechanical behavior of chemically reduced graphene oxide and multi-walled carbon nanotube hybrid material, Nanoscale Res Lett 11 (2016) 1–7.

[56] H. Li, K. Wu, Z. Xu, Z. Wang, Y. Meng, L. Li, Ultrahigh-Sensitivity Piezoresistive Pressure Sensors for Detection of Tiny Pressure, ACS Appl Mater Interfaces 10 (2018) 20826–20834. https://doi.org/10.1021/acsami.8b03639.

[57] Q. Zheng, J. Lee, X. Shen, X. Chen, J.-K. Kim, Graphene-based wearable piezoresistive physical sensors, Materials Today 36 (2020) 158–179. https://doi.org/https://doi.org/10.1016/j.mattod.2019.12.004.

[58] W.P. Carey, B.R. Kowalski, Chemical piezoelectric sensor and sensor array characterization, Anal Chem 58 (1986) 3077–3084.

[59] Y. Deng, J. Zhao, Y. Yu, J. Gao, S. Zhao, J. Yuan, Q. Han, G. Cui, A novel strategy for the simultaneous discrimination of dopamine and epinephrine by cyclic square wave voltammetry implemented with a customized potentiostat, New Journal of Chemistry 47 (2023) 12759–12769. https://doi.org/10.1039/D3NJ01376F.

[60] S. Peng, Y. Yu, S. Wu, C.-H. Wang, Conductive Polymer Nanocomposites for Stretchable Electronics: Material Selection, Design, and Applications, ACS Appl Mater Interfaces 13 (2021) 43831–43854. https://doi.org/10.1021/acsami.1c15014.

[61] D. Qi, K. Zhang, G. Tian, B. Jiang, Y. Huang, Stretchable Electronics Based on PDMS Substrates, Advanced Materials 33 (2021) 2003155. https://doi.org/https://doi.org/10.1002/adma.202003155.

[62] J C Lötters, W Olthuis, P H Veltink, P Bergveld, The mechanical properties of the rubber elastic polymer polydimethylsiloxane for sensor applications, Journal of Micromechanics and Microengineering 7 (1997) 145. https://doi.org/10.1088/0960-1317/7/3/017.

[63] V.-T. Nguyen, B.K. Min, Y. Yi, S.J. Kim, C.-G. Choi, MXene(Ti3C2TX)/graphene/PDMS composites for multifunctional broadband electromagnetic interference shielding skins, Chemical Engineering Journal 393 (2020) 124608. https://doi.org/https://doi.org/10.1016/j.cej.2020.124608.

[64] K. Parida, G. Thangavel, G. Cai, X. Zhou, S. Park, J. Xiong, P.S. Lee, Extremely stretchable and self-healing conductor based on thermoplastic elastomer for all-three-dimensional printed triboelectric nanogenerator, Nat Commun 10 (2019) 2158.

[65] Z. Wang, X. Guan, H. Huang, H. Wang, W. Lin, Z. Peng, Full 3D printing of stretchable piezoresistive sensor with hierarchical porosity and multimodulus architecture, Adv Funct Mater 29 (2019) 1807569.

[66] H. Sun, Z. Han, N. Willenbacher, Ultrastretchable conductive elastomers with a low percolation threshold for printed soft electronics, ACS Appl Mater Interfaces 11 (2019) 38092–38102.

[67] W. Yan, J. Li, G. Zhang, L. Wang, D. Ho, A synergistic self-assembled 3D PEDOT: PSS/graphene composite sponge for stretchable microsupercapacitors, J Mater Chem A Mater 8 (2020) 554–564.

[68] Y. Zhou, K. Maleski, B. Anasori, J.O. Thostenson, Y. Pang, Y. Feng, K. Zeng, C.B. Parker, S. Zauscher, Y. Gogotsi, Ti3C2T x MXene-reduced graphene oxide composite electrodes for stretchable supercapacitors, ACS Nano 14 (2020) 3576–3586.

[69] S. Fu, Z. Sun, P. Huang, Y. Li, N. Hu, Some basic aspects of polymer nanocomposites: A critical review, Nano Materials Science 1 (2019) 2–30.

[70] Y. Zhai, Y. Yu, K. Zhou, Z. Yun, W. Huang, H. Liu, Q. Xia, K. Dai, G. Zheng, C. Liu, Flexible and wearable carbon black/thermoplastic polyurethane foam with a pinnate-veined aligned porous structure for multifunctional piezoresistive sensors, Chemical Engineering Journal 382 (2020) 122985.

[71] D.J. Lipomi, M. Vosgueritchian, B.C.-K. Tee, S.L. Hellstrom, J.A. Lee, C.H. Fox, Z. Bao, Skin-like pressure and strain sensors based on transparent elastic films of carbon nanotubes, Nat Nanotechnol 6 (2011) 788–792. https://doi.org/10.1038/nnano.2011.184.

[72] S. Wu, S. Peng, C.H. Wang, Stretchable strain sensors based on PDMS composites with cellulose sponges containing one- and two-dimensional nanocarbons, Sens Actuators A Phys 279 (2018) 90–100. https://doi.org/https://doi.org/10.1016/j.sna.2018.06.002.

[73] R.B. Ladani, S. Wu, A.J. Kinloch, K. Ghorbani, J. Zhang, A.P. Mouritz, C.H. Wang, Improving the toughness and electrical conductivity of epoxy nanocomposites by using aligned carbon nanofibres, Compos Sci Technol 117 (2015) 146–158. https://doi.org/https://doi.org/10.1016/j.compscitech.2015.06.006.

[74] S. Wu, J. Zhang, R.B. Ladani, A.R. Ravindran, A.P. Mouritz, A.J. Kinloch, C.H. Wang, Novel Electrically Conductive Porous PDMS/Carbon Nanofiber Composites for Deformable Strain Sensors and Conductors, ACS Appl Mater Interfaces 9 (2017) 14207–14215. https://doi.org/10.1021/acsami.7b00847.

[75] N. Liu, A. Chortos, T. Lei, L. Jin, T.R. Kim, W.-G. Bae, C. Zhu, S. Wang, R. Pfattner, X. Chen, Ultratransparent and stretchable graphene electrodes, Sci Adv 3 (2017) e1700159.

[76] S.K. Tiwari, S. Sahoo, N. Wang, A. Huczko, Graphene research and their outputs: Status and prospect, Journal of Science: Advanced Materials and Devices 5 (2020) 10–29. https://doi.org/https://doi.org/10.1016/j.jsamd.2020.01.006.

[77] K.S. Novoselov, V.I. Fal′ko, L. Colombo, P.R. Gellert, M.G. Schwab, K. Kim, A roadmap for graphene, Nature 490 (2012) 192–200. https://doi.org/10.1038/nature11458.

[78] L. Qiu, J.Z. Liu, S.L.Y. Chang, Y. Wu, D. Li, Biomimetic superelastic graphene-based cellular monoliths, Nat Commun 3 (2012) 1241.

[79] S. Wu, R.B. Ladani, J. Zhang, K. Ghorbani, X. Zhang, A.P. Mouritz, A.J. Kinloch, C.H. Wang, Strain Sensors with Adjustable Sensitivity by Tailoring the Microstructure of Graphene Aerogel/PDMS Nanocomposites, ACS Appl Mater Interfaces 8 (2016) 24853–24861. https://doi.org/10.1021/acsami.6b06012.

[80] F. Xu, R. Chen, Z. Lin, Y. Qin, Y. Yuan, Y. Li, X. Zhao, M. Yang, X. Sun, S. Wang, Q. Peng, Y. Li, X. He, Superflexible Interconnected Graphene Network Nanocomposites for High-Performance Electromagnetic Interference Shielding, ACS Omega 3 (2018) 3599–3607. https://doi.org/10.1021/acsomega.8b00432.

[81] B. Anasori, M.R. Lukatskaya, Y. Gogotsi, 2D metal carbides and nitrides (MXenes) for energy storage, Nat Rev Mater 2 (2017) 16098. https://doi.org/10.1038/natrevmats.2016.98.

[82] M. Alhabeb, K. Maleski, B. Anasori, P. Lelyukh, L. Clark, S. Sin, Y. Gogotsi, Guidelines for Synthesis and Processing of Two-Dimensional Titanium Carbide (Ti3C2Tx MXene), Chemistry of Materials 29 (2017) 7633–7644. https://doi.org/10.1021/acs.chemmater.7b02847.

[83] S. Zhao, H.-B. Zhang, J.-Q. Luo, Q.-W. Wang, B. Xu, S. Hong, Z.-Z. Yu, Highly Electrically Conductive Three-Dimensional Ti3C2Tx MXene/Reduced Graphene Oxide Hybrid Aerogels with Excellent Electromagnetic Interference Shielding Performances, ACS Nano 12 (2018) 11193–11202. https://doi.org/10.1021/acsnano.8b05739.

[84] Y. Lu, X. Qu, W. Zhao, Y. Ren, W. Si, W. Wang, Q. Wang, W. Huang, X. Dong, Highly Stretchable, Elastic, and Sensitive MXene-Based Hydrogel for Flexible Strain and Pressure Sensors, Research 2020 (2024). https://doi.org/10.34133/2020/2038560.

[85] X.-P. Li, Y. Li, X. Li, D. Song, P. Min, C. Hu, H.-B. Zhang, N. Koratkar, Z.-Z. Yu, Highly sensitive, reliable and flexible piezoresistive pressure sensors featuring polyurethane sponge coated with MXene sheets, J Colloid Interface Sci 542 (2019) 54–62. https://doi.org/https://doi.org/10.1016/j.jcis.2019.01.123.

[86] A.M. Dimiev, A. Khannanov, I. Vakhitov, A. Kiiamov, K. Shukhina, J.M. Tour, Revisiting the mechanism of oxidative unzipping of multiwall carbon nanotubes to graphene nanoribbons, ACS Nano 12 (2018) 3985–3993.

[87] Y. Jun, S. Habibpour, M. Hamidinejad, M.G. Park, W. Ahn, A. Yu, C.B. Park, Enhanced electrical and mechanical properties of graphene nano-ribbon/thermoplastic polyurethane composites, Carbon N Y 174 (2021) 305–316. https://doi.org/https://doi.org/10.1016/j.carbon.2020.12.023.

[88] H.J. Lee, J.C. Yang, J. Choi, J. Kim, G.S. Lee, S.P. Sasikala, G.-H. Lee, S.-H.K. Park, H.M. Lee, J.Y. Sim, S. Park, S.O. Kim, Hetero-Dimensional 2D Ti3C2Tx MXene and 1D Graphene Nanoribbon Hybrids for Machine Learning-Assisted Pressure Sensors, ACS Nano 15 (2021) 10347–10356. https://doi.org/10.1021/acsnano.1c02567.

[89] J. Yan, C.E. Ren, K. Maleski, C.B. Hatter, B. Anasori, P. Urbankowski, A. Sarycheva, Y. Gogotsi, Flexible MXene/graphene films for ultrafast supercapacitors with outstanding volumetric capacitance, Adv Funct Mater 27 (2017) 1701264.

[90] E. Planes, L. Flandin, N. Alberola, Polymer Composites Bipolar Plates for PEMFCs, Energy Procedia 20 (2012) 311–323. https://doi.org/https://doi.org/10.1016/j.egypro.2012.03.031.

[91] Z. Jin, K.P. Pramoda, G. Xu, S.H. Goh, Dynamic mechanical behavior of melt-processed multi-walled carbon nanotube/poly(methyl methacrylate) composites, Chem Phys Lett 337 (2001) 43–47. https://doi.org/10.1016/S0009-2614(01)00186-5.

[92] R. Haggenmueller, H.H. Gommans, A.G. Rinzler, J.E. Fischer, K.I. Winey, Aligned single-wall carbon nanotubes in composites by melt processing methods, Chem Phys Lett 330 (2000) 219–225. https://doi.org/10.1016/S0009-2614(00)01013-7.

[93] A.R. Bhattacharyya, T. V. Sreekumar, T. Liu, S. Kumar, L.M. Ericson, R.H. Hauge, R.E. Smalley, Crystallization and orientation studies in polypropylene/single wall carbon nanotube composite, Polymer (Guildf) 44 (2003) 2373–2377. https://doi.org/10.1016/S0032-3861(03)00073-9.

[94] S.-W. Dai, Y.-L. Gu, L. Zhao, W. Zhang, C.-H. Gao, Y.-X. Wu, S.-C. Shen, C. Zhang, T.-T. Kong, Y.-T. Li, Bamboo-inspired mechanically flexible and electrically conductive polydimethylsiloxane foam materials with designed hierarchical pore structures for ultra-sensitive and reliable piezoresistive pressure sensor, Compos B Eng 225 (2021) 109243.

[95] Y. Pang, H. Tian, L. Tao, Y. Li, X. Wang, N. Deng, Y. Yang, T.-L. Ren, Flexible, Highly Sensitive, and Wearable Pressure and Strain Sensors with Graphene Porous Network Structure, ACS Appl Mater Interfaces 8 (2016) 26458–26462. https://doi.org/10.1021/acsami.6b08172.

[96] N. Luo, Y. Huang, J. Liu, S. Chen, C.P. Wong, N. Zhao, Hollow-structured graphene–silicone-composite-based piezoresistive sensors: Decoupled property tuning and bending reliability, Advanced Materials 29 (2017) 1702675.

[97] L.A. Kurup, J.N. Arthur, S.D. Yambem, Highly Sensitive Capacitive Low-Pressure Graphene Porous Foam Sensors, ACS Appl Electron Mater 4 (2022) 3962–3972.

[98] D. Sengupta, Y. Pei, A.G.P. Kottapalli, Ultralightweight and 3D squeezable graphene-polydimethylsiloxane composite foams as piezoresistive sensors, ACS Appl Mater Interfaces 11 (2019) 35201–35211.

[99] L. Wang, Z. Ma, Y. Zhang, L. Chen, D. Cao, J. Gu, Polymer-based EMI shielding composites with 3D conductive networks: a mini-review, SusMat 1 (2021) 413–431.

[100] X. Fan, G. Zhang, Q. Gao, J. Li, Z. Shang, H. Zhang, Y. Zhang, X. Shi, J. Qin, Highly expansive, thermally insulating epoxy/Ag nanosheet composite foam for electromagnetic interference shielding, Chemical Engineering Journal 372 (2019) 191–202.

[101] Y. Fei, F. Chen, W. Fang, A. Hejna, L. Xu, T. Liu, M. Zhong, J. Yang, T. Kuang, Conductive thermoplastic polyurethane nanocomposite foams derived from a cellulose/MWCNTs aerogel framework: simultaneous enhancement of piezoresistance, strength, and endurance, J Mater Chem C Mater 9 (2021) 13103–13114.

[102] Y. Ding, T. Xu, O. Onyilagha, H. Fong, Z. Zhu, Recent Advances in Flexible and Wearable Pressure Sensors Based on Piezoresistive 3D Monolithic Conductive Sponges, ACS Appl Mater Interfaces 11 (2019) 6685–6704. https://doi.org/10.1021/acsami.8b20929.

[103] M. Cao, J. Su, S. Fan, H. Qiu, D. Su, L. Li, Wearable piezoresistive pressure sensors based on 3D graphene, Chemical Engineering Journal 406 (2021) 126777.

[104] C. Huang, Y. Wang, Y. Cheng, Z. Qi, A. Liu, Q. Deng, N. Hu, Naturally dried superelastic bioinspired graphene aerogel for pressure/stretch sensing and separation, Compos Sci Technol 226 (2022) 109549.

[105] M. Wang, X. Duan, Y. Xu, X. Duan, Functional Three-Dimensional Graphene/Polymer Composites, ACS Nano 10 (2016) 7231–7247. https://doi.org/10.1021/acsnano.6b03349.

[106] P. Simon, Y. Gogotsi, Materials for electrochemical capacitors, Nat Mater 7 (2008) 845–854. https://doi.org/10.1038/nmat2297.

[107] S. Mao, G. Lu, J. Chen, Three-dimensional graphene-based composites for energy applications, Nanoscale 7 (2015) 6924–6943.

[108] B. Zhao, C. Zhao, M. Hamidinejad, C. Wang, R. Li, S. Wang, K. Yasamin, C.B. Park, Incorporating a microcellular structure into PVDF/graphene–nanoplatelet composites to tune their electrical conductivity and electromagnetic interference shielding properties, J Mater Chem C Mater 6 (2018) 10292–10300.

[109] J. Cheng, C. Li, Y. Xiong, H. Zhang, H. Raza, S. Ullah, J. Wu, G. Zheng, Q. Cao, D. Zhang, Q. Zheng, R. Che, Recent Advances in Design Strategies and Multifunctionality of Flexible Electromagnetic Interference Shielding Materials, Nanomicro Lett 14 (2022) 80. https://doi.org/10.1007/s40820-022-00823-7.

[110] B. Zhao, C. Zhao, R. Li, S.M. Hamidinejad, C.B. Park, Flexible, ultrathin, and high-efficiency electromagnetic shielding properties of poly (vinylidene fluoride)/carbon composite films, ACS Appl Mater Interfaces 9 (2017) 20873–20884.

[111] S. Naeem, V. Baheti, V. Tunakova, J. Militky, D. Karthik, B. Tomkova, Development of porous and electrically conductive activated carbon web for effective EMI shielding applications, Carbon N Y 111 (2017) 439–447.

[112] M.H. Al-Saleh, U. Sundararaj, Electromagnetic interference shielding mechanisms of CNT/polymer composites, Carbon N Y 47 (2009) 1738–1746.

[113] D.C. Marcano, D. V. Kosynkin, J.M. Berlin, A. Sinitskii, Z. Sun, A. Slesarev, L.B. Alemany, W. Lu, J.M. Tour, Improved synthesis of graphene oxide, ACS Nano 4 (2010) 4806–4814. https://doi.org/10.1021/nn1006368.

[114] Y. Ma, Y. Yue, H. Zhang, F. Cheng, W. Zhao, J. Rao, S. Luo, J. Wang, X. Jiang, Z. Liu, N. Liu, Y. Gao, 3D Synergistical MXene/Reduced Graphene Oxide Aerogel for a Piezoresistive Sensor, ACS Nano 12 (2018) 3209–3216. https://doi.org/10.1021/acsnano.7b06909.

[115] H. Liu, W. Huang, J. Gao, K. Dai, G. Zheng, C. Liu, C. Shen, X. Yan, J. Guo, Z. Guo, Piezoresistive behavior of porous carbon nanotube-thermoplastic polyurethane conductive nanocomposites with ultrahigh compressibility, Appl Phys Lett 108 (2016) 1–5. https://doi.org/10.1063/1.4939265.

[116] Z. Yu, T. Dai, S. Yuan, H. Zou, P. Liu, Electromagnetic Interference Shielding Performance of Anisotropic Polyimide/Graphene Composite Aerogels, ACS Appl Mater Interfaces 12 (2020) 30990–31001. https://doi.org/10.1021/acsami.0c07122.

[117] L. Wang, M. Wu, Q. Ren, Z. Weng, W. Li, X. Zhu, W. Zheng, X. Yi, Strong and high void fraction PP/CNS nanocomposite foams fabricated by core-back foam injection molding, J Appl Polym Sci 140 (2023) 1–10. https://doi.org/10.1002/app.53521.

[118] S. Habibpour, J.G. Um, Y.-S. Jun, P. Bhargava, C.B. Park, A. Yu, Structural Impact of Graphene Nanoribbon on Mechanical Properties and Anti-corrosion Performance of Polyurethane Nanocomposites, Chemical Engineering Journal 405 (2021). https://doi.org/10.1016/j.cej.2020.126858.

[119] F. Yang, D. Presto, Y. Pan, K. Liu, L. Zhou, S. Narayanan, Y. Zhu, Z. Peng, M.D. Soucek, M. Tsige, M.D. Foster, Proximity to Graphene Dramatically Alters Polymer Dynamics, Macromolecules 52 (2019) 5074–5085. https://doi.org/10.1021/acs.macromol.9b00317.

[120] S. Pei, H.M. Cheng, The reduction of graphene oxide, Carbon N Y 50 (2012) 3210–3228. https://doi.org/10.1016/j.carbon.2011.11.010.

[121] Y.H. Kang, E.J. Bae, M.H. Lee, M. Han, B.J. Kim, S.Y. Cho, Highly Flexible and Durable Thermoelectric Power Generator Using CNT/PDMS Foam by Rapid Solvent Evaporation, Small 18 (2022) 1–8. https://doi.org/10.1002/smll.202106108.

[122] M.H. Lee, Y.H. Kang, J. Kim, Y.K. Lee, S.Y. Cho, Freely Shapable and 3D Porous Carbon Nanotube Foam Using Rapid Solvent Evaporation Method for Flexible Thermoelectric Power Generators, Adv Energy Mater 9 (2019) 1–9. https://doi.org/10.1002/aenm.201900914.

[123] X. Lu, A. Zhang, O. Dubrunfaut, D. He, L. Pichon, J. Bai, Numerical modeling and experimental characterization of the AC conductivity and dielectric properties of CNT/polymer nanocomposites, Compos Sci Technol 194 (2020) 108150. https://doi.org/10.1016/j.compscitech.2020.108150.

[124] Y. seok Jun, S. Habibpour, M. Hamidinejad, M.G. Park, W. Ahn, A. Yu, C.B. Park, Enhanced electrical and mechanical properties of graphene nano-ribbon/thermoplastic polyurethane composites, Carbon N Y 174 (2021) 305–316. https://doi.org/10.1016/j.carbon.2020.12.023.

[125] B. Zhao, C. Zhao, M. Hamidinejad, C. Wang, R. Li, S. Wang, K. Yasamin, C.B. Park, Incorporating a microcellular structure into PVDF/graphene-nanoplatelet composites to tune their electrical conductivity and electromagnetic interference shielding properties, J Mater Chem C Mater 6 (2018) 10292–10300. https://doi.org/10.1039/C8TC03714K.

[126] S. Wang, Y. Huang, E. Chang, C. Zhao, A. Ameli, H.E. Naguib, C.B. Park, Evaluation and modeling of electrical conductivity in conductive polymer nanocomposite foams with multiwalled carbon nanotube networks, Chemical Engineering Journal 411 (2021) 128382. https://doi.org/10.1016/j.cej.2020.128382.

[127] S. Barrau, P. Demont, A. Peigney, C. Laurent, C. Lacabanne, Dc and ac conductivity of carbon nanotubes-polyepoxy composites, Macromolecules 36 (2003) 5187–5194. https://doi.org/10.1021/ma021263b.

[128] P.C. Ma, M.Y. Liu, H. Zhang, S.Q. Wang, R. Wang, K. Wang, Y.K. Wong, B.Z. Tang, S.H. Hong, K.W. Paik, J.K. Kim, Enhanced electrical conductivity of nanocomposites containing hybrid fillers of carbon nanotubes and carbon black, ACS Appl Mater Interfaces 1 (2009) 1090–1096. https://doi.org/10.1021/am9000503.

[129] M. Jebli, C. Rayssi, J. Dhahri, M. Ben Henda, H. Belmabrouk, A. Bajahzar, Structural and morphological studies, and temperature/frequency dependence of electrical conductivity of Ba0.97La0.02Ti1−xNb4x/5O3perovskite ceramics, RSC Adv 11 (2021) 23664–23678. https://doi.org/10.1039/d1ra01763b.

[130] S. Habibpour, K. Zarshenas, M. Zhang, M. Hamidinejad, L. Ma, C.B. Park, A. Yu, Greatly Enhanced Electromagnetic Interference Shielding Effectiveness and Mechanical Properties of Polyaniline-Grafted Ti3C2TxMXene-PVDF Composites, ACS Appl Mater Interfaces (2022). https://doi.org/10.1021/acsami.2c03121.

[131] L. Ma, M. Hamidinejad, C. Liang, B. Zhao, S. Habibpour, A. Yu, T. Filleter, C.B. Park, Enhanced electromagnetic wave absorption performance of polymer/SiC-nanowire/MXene (Ti3C2Tx) composites, Carbon N Y 179 (2021) 408–416.

[132] X. Xia, Z. Zhong, G.J. Weng, Maxwell–Wagner–Sillars mechanism in the frequency dependence of electrical conductivity and dielectric permittivity of graphene-polymer nanocomposites, Mechanics of Materials 109 (2017) 42–50. https://doi.org/https://doi.org/10.1016/j.mechmat.2017.03.014.

[133] D.M. Edwards, M.I. Katsnelson, High-temperature ferromagnetism of sp electrons in narrow impurity bands: application to CaB6, Journal of Physics: Condensed Matter 18 (2006) 7209. https://doi.org/10.1088/0953-8984/18/31/016.

[134] H. Santos, L. Chico, J.E. Alvarellos, A. Latgé, Defect-enhanced Rashba spin-polarized currents in carbon nanotubes, Phys Rev B 96 (2017) 165401. https://doi.org/10.1103/PhysRevB.96.165401.

[135] T.M. Levitskaya, B.K. Sternberg, Electrical Spectroscopy of Earth Materials, Elsevier, 2019.

[136] M. Salari, S. Habibpour, M. Hamidinejad, S.M. Taromsari, H.E. Naguib, A. Yu, C.B. Park, Enhanced electrical properties of microcellular polymer nanocomposites via nanocarbon geometrical alteration: a comparison of graphene nanoribbons and their parent multiwalled carbon nanotubes, Mater Horiz (2023).

[137] M. Hamidinejad, M. Salari, L. Ma, N. Moghimian, B. Zhao, H.K. Taylor, T. Filleter, C.B. Park, Electrically and thermally graded microcellular polymer/graphene nanoplatelet composite foams and their EMI shielding properties, Carbon N Y 187 (2022) 153–164.

[138] L.T. Vo, S.H. Anastasiadis, E.P. Giannelis, Dielectric study of poly (styrene-co-butadiene) composites with carbon black, silica, and nanoclay, Macromolecules 44 (2011) 6162–6171.

[139] Z. Sang, K. Ke, I. Manas-Zloczower, Design strategy for porous composites aimed at pressure sensor application, Small 15 (2019) 1903487.

[140] Y. Li, J. Chen, L. Huang, C. Li, J.D. Hong, G. Shi, Highly compressible macroporous graphene monoliths via an improved hydrothermal process, Advanced Materials 26 (2014) 4789–4793. https://doi.org/10.1002/adma.201400657.

[141] Y. Long, X. Zhao, X. Jiang, L. Zhang, H. Zhang, Y. Liu, H. Zhu, A porous graphene/polydimethylsiloxane composite by chemical foaming for simultaneous tensile and compressive strain sensing, FlatChem 10 (2018) 1–7. https://doi.org/https://doi.org/10.1016/j.flatc.2018.07.001.

[142] H. Liu, M. Dong, W. Huang, J. Gao, K. Dai, J. Guo, G. Zheng, C. Liu, C. Shen, Z. Guo, Lightweight conductive graphene/thermoplastic polyurethane foams with ultrahigh compressibility for piezoresistive sensing, J Mater Chem C Mater 5 (2017) 73–83. https://doi.org/10.1039/C6TC03713E.

[143] L. Zhao, F. Qiang, S.-W. Dai, S.-C. Shen, Y.-Z. Huang, N.-J. Huang, G.-D. Zhang, L.-Z. Guan, J.-F. Gao, Y.-H. Song, L.-C. Tang, Construction of sandwich-like porous structure of graphene-coated foam composites for ultrasensitive and flexible pressure sensors, Nanoscale 11 (2019) 10229–10238. https://doi.org/10.1039/C9NR02672J.

[144] J. Yang, Y. Ye, X. Li, X. Lü, R. Chen, Flexible, conductive, and highly pressure-sensitive graphene-polyimide foam for pressure sensor application, Compos Sci Technol 164 (2018) 187–194. https://doi.org/https://doi.org/10.1016/j.compscitech.2018.05.044.

[145] D. Sengupta, Y. Pei, A.G.P. Kottapalli, Ultralightweight and 3D Squeezable Graphene-Polydimethylsiloxane Composite Foams as Piezoresistive Sensors, ACS Appl Mater Interfaces 11 (2019) 35201–35211. https://doi.org/10.1021/acsami.9b11776.

[146] Y. Luo, Q. Xiao, B. Li, Highly compressible graphene/polyurethane sponge with linear and dynamic piezoresistive behavior, RSC Adv 7 (2017) 34939–34944. https://doi.org/10.1039/C7RA03922K.

[147] Y. Qin, Q. Peng, Y. Ding, Z. Lin, C. Wang, Y. Li, F. Xu, J. Li, Y. Yuan, X. He, Y. Li, Lightweight, Superelastic, and Mechanically Flexible Graphene/Polyimide Nanocomposite Foam for Strain Sensor Application, ACS Nano 9 (2015) 8933–8941. https://doi.org/10.1021/acsnano.5b02781.